Original

Scheifele, B.; Waterman, S.; Carpenter, J.:
Turbulence and Mixing in the Arctic Ocean's Amundsen Gulf.
In: Journal of Physical Oceanography. Vol. 51 (2021) 1, 169 - 186.
First published online by AMS: 15.10.2020

https://dx.doi.org/10.1175/JPO-D-20-0057.1

Turbulence and Mixing in the Arctic Ocean's Amundsen Gulf

BENJAMIN SCHEIFELE,[a] STEPHANIE WATERMAN,[a] AND JEFFREY R. CARPENTER[b]

[a] *Department of Earth, Ocean and Atmospheric Sciences, University of British Columbia, Vancouver, British Columbia, Canada*
[b] *Institute of Coastal Research, Helmholtz-Zentrum Geesthacht, Geesthacht, Germany*

(Manuscript received 12 March 2020, in final form 3 September 2020)

ABSTRACT: This study uses CTD and microstructure measurements of shear and temperature from 348 glider profiles to characterize turbulence and turbulent mixing in the southeastern Beaufort Sea, where turbulence observations are presently scarce. We find that turbulence is typically weak: the turbulent kinetic energy dissipation rate ε has a median value (with 95% confidence intervals in parentheses) of 2.3 [2.2, 2.4] $\times 10^{-11}$ W kg^{-1} and is less than 1.0×10^{-10} W kg^{-1} in 68% of observations. Variability in ε spans five orders of magnitude, with indications that turbulence is bottom enhanced and modulated in time by the semidiurnal tide. Stratification is strong and frequently damps turbulence, inhibiting diapycnal mixing. Buoyancy Reynolds number estimates suggest that turbulent diapycnal mixing is unlikely in 93% of observations; however, a small number of strongly turbulent mixing events are disproportionately important in determining net buoyancy fluxes. The arithmetic mean diapycnal diffusivity of density is 4.5 [2.3, 14] $\times 10^{-6}$ m^2 s^{-1}, three orders of magnitude larger than that expected from molecular diffusion. Vertical heat fluxes are modest at $O(0.1)$ W m^{-2}, of the same order of magnitude as those in the Canada Basin double-diffusive staircase, however, staircases are generally not observed. Despite significant heat present in the Pacific Water layer in the form of a warm-core mesoscale eddy and smaller, $O(1)$ km, temperature anomalies, turbulent mixing was found to be too low to release this heat to shallower depths.

KEYWORDS: Arctic; Mixing; Turbulence; In situ oceanic observations; Profilers, oceanic

1. Introduction

In this study, we present observations of ocean turbulence and mixing in the Beaufort Sea's Amundsen Gulf in the western Arctic Ocean (Fig. 1) from a series of conductivity–temperature–depth (CTD) and microstructure measurements collected in summer 2015. The Amundsen Gulf is the site of the Cape Bathurst polynya, part of the circum-Arctic system of flaw polynyas that are important in the dynamics of the Arctic ice sheet, the formation of Arctic deep water, and, in the case of the Cape Bathurst polynya, as a habitat for some of the highest densities of birds and mammals found anywhere in the Arctic (Arrigo and van Dijken 2004; Harwood and Stirling 1992; Dickson and Gilchrist 2002). It is also strategically located along the Northwest Passage and is expected to become a major commercial shipping line as summer sea ice continues to decrease (Prowse et al. 2009; Khon et al. 2010). Since the late 1990s, there has been a dramatic reduction in the extent and age of multiyear sea ice in the region, as well as large interannual variations in summer ice concentration and the duration of summertime ice clearance (Niemi et al. 2012). Over the whole Arctic, changes in sea ice alongside other rapid and dramatic Arctic system changes in the past few decades have perturbed regional ecosystems at all tropic levels (e.g., Grebmeier et al. 2006; Wassmann 2011, 2015) and have the potential to affect ecosystem services related to natural resources, food production, climate regulation, and cultural integrity (Post et al. 2009). In light of these ongoing changes to the broader physical environment, it is important to continue developing a detailed understanding of the physical oceanography and, in particular, the mixing characteristics of the region to facilitate studies that will model the environmental and ecological responses to future regional climate change (e.g., Carmack and MacDonald 2002; Rainville et al. 2011; Carmack et al. 2015).

The Arctic Ocean is undersampled with respect to turbulence and mixing rates, and observations of ocean turbulence are notably scarce in the Beaufort Sea. A number of studies over the previous decade have deepened our understanding of mixing rates and mechanisms in the broader Canada Basin (e.g., Rainville and Winsor 2008; Timmermans et al. 2008a,b; Guthrie et al. 2013; Dosser et al. 2014; Shaw and Stanton 2014; Chanona et al. 2018), but, to our knowledge, only six previous studies (Padman and Dillon 1987; Bourgault et al. 2011; Shroyer 2012; Rippeth et al. 2015; Lincoln et al. 2016; Fine et al. 2018) have used microstructure measurements to characterize mixing rates in the Beaufort Sea directly. Many of these studies have focused on specific processes such as diffusive convection (Padman and Dillon 1987), mesoscale eddy heat loss (Fine et al. 2018), and canyon flows (Shroyer 2012). Outside of these, the studies collectively confirm that turbulence in the Beaufort Sea is generally very weak and mixing rates are generally very small away from the surface and significant topography. This is consistent with the indirect estimates of Guthrie et al. (2013) that report internal wave energies and consequent background mixing rates that are lower by about a factor of 5 in the Beaufort Sea than in the central and eastern Arctic Ocean. Lincoln et al. (2016) attribute the suppression of turbulent mixing at intermediate depths to the strong stratification that characterizes the central Canada Basin, which was observed to buffer intermediate depths from enhanced wind-driven internal wave energy. At the same time, a number of observations also suggest a key role of topography, and in particular the steep topography of the basin margins and of canyons, in

Corresponding author: Stephanie Waterman, swaterman@eoas.ubc.ca

DOI: 10.1175/JPO-D-20-0057.1

© 2021 American Meteorological Society. For information regarding reuse of this content and general copyright information, consult the AMS Copyright Policy (www.ametsoc.org/PUBSReuseLicenses).

Brought to you by HELMHOLTZ-ZENTRUM HEREON | Unauthenticated | Downloaded 04/22/21 12:14 PM UTC

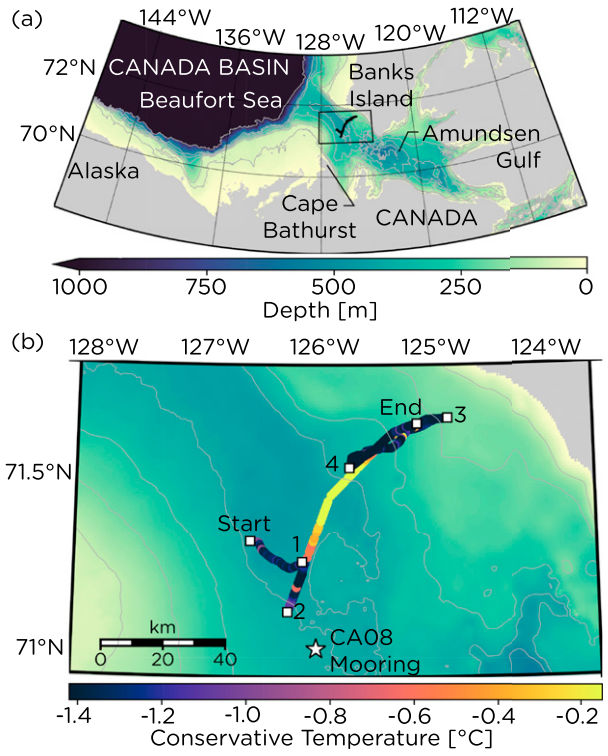

FIG. 1. (a) Map of the southeastern Beaufort Sea, showing the location of Amundsen Gulf. The glider path is shown by the thin black line inside the black-outlined rectangle. (b) Enlarged view of the region enclosed by the black-outlined rectangle in (a), showing the path of the glider. The start and end locations of the track are shown by the white rectangles; four intermediate waypoints are also shown and are numbered consecutively. The color on the glider's track-line is Conservative Temperature along the 1026.15 kg m^{-3} isopycnal, indicating the location and spatial scale of the warm-core eddy discussed in the text (section 5c). The white star is the location of ArcticNet mooring CA08. Bathymetry data are from IBCAO 3.0 (Jakobsson et al. 2012).

driving a localized enhancement of turbulence and mixing (Shroyer 2012; Rippeth et al. 2015; Lincoln et al. 2016). In addition, an important role of mesoscale eddy features in modulating the space and time variability in mixing rates has been documented (Fine et al. 2018). There remains a pressing need to continue building a broad record of mixing estimates in the region to better understand the space and time geography of mixing rates and mechanisms, and their susceptibility to change.

With this study, we contribute to a more comprehensive understanding of the mixing environment within Amundsen Gulf of the southeastern Beaufort Sea by providing a novel description of the region's turbulence and mixing characteristics. By using an autonomous ocean glider equipped with a CTD and turbulence sensors, we collected a large number of tightly resolved measurements of turbulent microstructure shear and temperature gradients, concurrent with observations of the hydrography, made possible by the long-duration, continuous, high-frequency sampling capabilities of the glider platform. This novel mode of sampling is significant because a large number of tightly resolved measurements are needed to accurately characterize turbulence, which tends to be described with intermittent, lognormally distributed variables that are easily undersampled (Baker and Gibson 1987; Gregg 1987). Further, it permits an examination of high-frequency time and space patterns that are difficult to resolve with traditional turbulence sampling techniques. We use these measurements to characterize the statistical distributions of estimates of the turbulent dissipation rate of kinetic energy, diapycnal mixing rate, and vertical heat flux during the period of observation. In addition, we use these observations to gain insight into the relative importance of different mechanisms, namely, tidal mixing, double diffusion, and near-surface mesoscale and smaller processes, that underpin and/or modulate the observed turbulence environment. To our knowledge, this is the first time such a highly resolved characterization of mixing from direct turbulence measurements has been presented for this region, and the first time an autonomous instrument has been used to characterize the statistics of turbulence and mixing in the western Arctic Ocean.

The remainder of the document is structured as follows. In section 2, we describe the CTD and microstructure measurements from the glider, and briefly outline the data processing methods. Section 3 uses the CTD measurements to describe the relevant hydrographic context. In section 4, we present the primary results of this study, the turbulence observations and the mixing rate and heat flux estimates derived from them. Section 5 presents a discussion of mixing mechanisms. We synthesize our results in section 6.

2. Measurements and data processing

a. *Sampling strategy*

We collected CTD and turbulence measurements in Amundsen Gulf using an autonomous 1000-m-rated Teledyne Webb Slocum G2 ocean glider, fitted with 1) a pumped Sea-Bird CTD measuring conductivity, temperature, and pressure and 2) an externally mounted turbulence-sensing package measuring shear and temperature microstructure (section 2b). The measurements used in this study are those first described by Scheifele et al. (2018), collected continuously over 11 days during the period from 25 August to 5 September 2015.

The 186-km horizontal path of the glider, immediately northwest of the gulf's sill, is shown in Fig. 1. The glider spent the first 5 days in the central gulf, where the water depth exceeds 400 m, and the remaining time on three traverses of the continental shelf near Banks Island. Along this path, the glider collected 348 discrete quasi-vertical measurement profiles, at a nominal glide angle of 26° from the horizontal. The first 112 profiles, in water ~410 m deep, extend from the near surface to a fixed depth of 300 m; later profiles typically extend to within 15 m of the local bottom, which ranged between 205 and 430 m in depth. The location of each profile is approximated with its mean coordinates, neglecting horizontal translation that occurs over the course of one profile. The mean and standard deviation distances between consecutive profiles are 536 and 357 m, respectively.

Brought to you by HELMHOLTZ-ZENTRUM HEREON | Unauthenticated | Downloaded 04/22/21 12:14 PM UTC

b. Turbulence measurements and data processing

The glider carried an externally mounted, self-contained microstructure sensing package known as a *Microrider*, also used in recent studies by Fer et al. (2014), Peterson and Fer (2014), Palmer et al. (2015), and Schultze et al. (2017). The Microrider is manufactured by Rockland Scientific and is factory-installed on the glider. Our configuration of the Microrider had two velocity shear probes and two fast-response thermistors, each sampling at 512 Hz, measuring microstructure velocity and temperature gradients, respectively. All sensors sampled continuously during the deployment, but one of the two shear probes failed after the first three days of measurement.

We derive independent estimates of the turbulent kinetic energy (TKE) dissipation rate ε from each of the four microstructure channels. This rate is a measure of the intensity of turbulence in the flow and is proportional to the rate of diapycnal mixing in the Osborn (1980) model (see section 4c). We briefly outline our methods to derive ε from the shear and temperature microstructure measurements below; a more detailed description of the methods and their limitations is given in Scheifele et al. (2018).

We calculate the TKE dissipation rate from the measured microstructure shear variance according to

$$\varepsilon_U = 7.5\nu\left\langle\left(\frac{\partial u'}{\partial x}\right)^2\right\rangle, \tag{1}$$

where $\partial u'/\partial x$ is a turbulent-scale shear component measured along the glider's along-path coordinate x and ν is the kinematic viscosity of seawater. Here we have made the assumption of isotropic turbulence. Angled brackets indicate ensemble averaging over the segments and subsegments indicated below, and the subscript U indicates that this is a shear-derived dissipation rate estimate. We use half-overlapping 40-s segments of measurement to calculate successive ε_U estimates; within each of these segments, we calculate and average 19 shear power spectra from consecutive half-overlapping 4-s subsegments; we then integrate to obtain the shear variance in the segment. The spatial length encompassed by each 4-s subsegment depends on the glider's speed and has a mean (standard deviation) of 163 cm (15 cm) for upcasts and 100 cm (15 cm) for downcasts.

We calculate the TKE dissipation rate from the temperature microstructure measurements using power spectra of temperature gradients, calculated over the same 40-s segments and 4-s subsegments that we used to calculate the shear spectra. We fit a theoretical form for the temperature gradient spectrum (the Batchelor spectrum) to the observed temperature gradient power spectrum using the maximum likelihood estimator method outlined by Ruddick et al. (2000). In this procedure, ε is a variable fitting parameter that is optimized by minimizing the difference between the observed and theoretical spectra. We refer to this optimized value as ε_T, with the subscript T indicating a temperature gradient-derived dissipation rate estimate.

Both ε_U and ε_T estimates are then subjected to a series of quality control criteria that remove suspect estimates. These routines are designed to flag and remove values where, for example, the glider's flight was not steady, shear probes contacted small marine organisms or debris, Taylor's frozen turbulence hypothesis is violated in the calculation of power spectra, etc. They are detailed in Scheifele et al. (2018). Quality control removes 22% of ε_U estimates and 34% of ε_T estimates.

Dual estimates of ε from each set of probes are arithmetically averaged to obtain single ε_U and ε_T values for each 40-s segment. As described in detail in Scheifele et al. (2018), we find agreement within a factor of 2 from the two types of estimates when ε exceeds $3 \times 10^{-11}\,\mathrm{W\,kg^{-1}}$, a threshold we identify as the noise floor of the shear-derived estimates. However, our analysis indicates that the noise floor of the shear measurements biases the statistical distribution of ε_U at values of ε as large as $1 \times 10^{-10}\,\mathrm{W\,kg^{-1}}$, while temperature-derived estimates of ε are reliable to values as small as $2 \times 10^{-12}\,\mathrm{W\,kg^{-1}}$. The averaged ε_U and ε_T estimates are combined into a single best ε estimate using the following method. When $\varepsilon_U \geq 1 \times 10^{-10}\,\mathrm{W\,kg^{-1}}$, we keep only ε_U because the shear-derived estimate relies more directly on the definition of the dissipation rate and is more reliable in energetic conditions (Gregg 1999). However, if the ε_U estimate is unavailable because it failed quality control, we keep the coincident ε_T estimate instead, if this is available. If both are available, but they differ by more than a factor of 10, both are discarded. Below $1 \times 10^{-10}\,\mathrm{W\,kg^{-1}}$, we keep only ε_T. However, when $\varepsilon_T < 2 \times 10^{-12}\,\mathrm{W\,kg^{-1}}$, we set ε to zero, following the approach used by Gregg et al. (2012). We are left with 22 153 unique ε estimates for the remaining analysis; of these, 4699 (21%) are set to zero.

c. Arithmetic versus geometric averaging

Turbulence in the ocean is patchy in space and intermittent in time, and the distributions of dissipation rates and mixing coefficients are typically lognormal-like, spanning many orders of magnitude (Baker and Gibson 1987). Arithmetic mean values may differ from median and geometric mean values by orders of magnitude in such data, so it is important to distinguish between these various metrics and recognize their distinct physical interpretations (Kirkwood 1979). The geometric mean (GM) is defined as $\mathrm{GM} = \sqrt[N]{X_1 X_2 \cdots X_N}$ for a sample set $\{X_i\}$ with a sample size of N. This is equivalent to computing the mean of the logarithms of the samples and then taking the antilog. As such, the GM is a useful metric of the arithmetic mean for lognormal distributions, as it characterizes the distribution's central tendency, or "typical value." In the case of a lognormal distribution, the geometric mean is equal to the median value; the difference between the geometric mean and median can thus be interpreted as indicating the degree of departure from lognormality. In contrast, the arithmetic mean (AM), defined as $\mathrm{AM} = \sum_{i=1}^{N} X_i/N$, characterizes the integrated effect of the distribution. It is disproportionately skewed by a small number of large values on the right-hand side of the distribution in the case of lognormally distributed variables. Thus, while a geometric mean or median mixing rate represents the "typical" mixing rate in a set of observations, the arithmetic mean rate describes the cumulative effect of mixing, and thus better typifies, say, average buoyancy transformations produced by mixing in those observations. We present geometric mean, median and arithmetic mean values

Brought to you by HELMHOLTZ-ZENTRUM HEREON | Unauthenticated | Downloaded 04/22/21 12:14 PM UTC

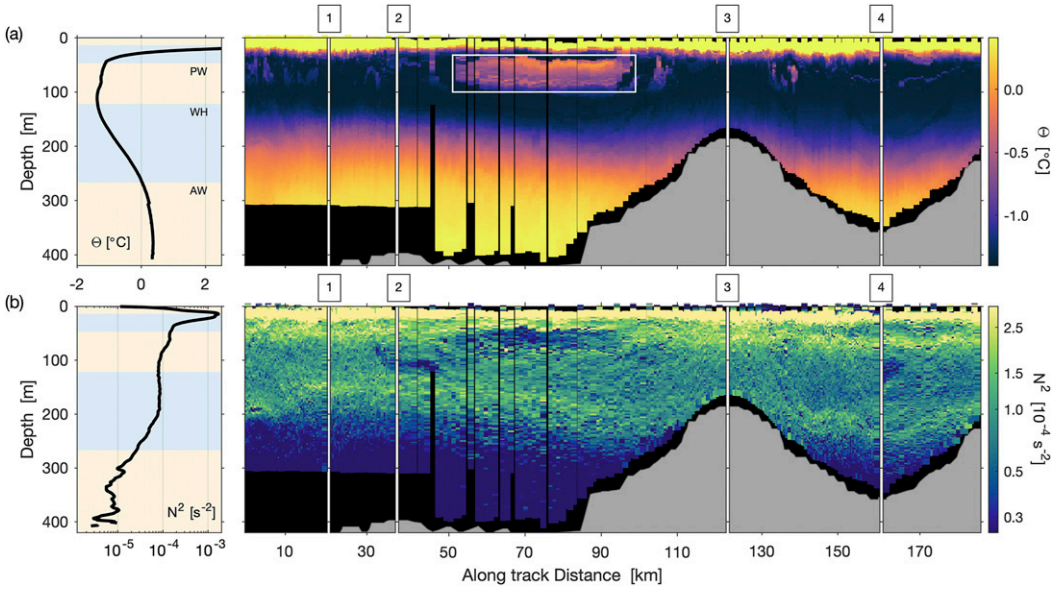

FIG. 2. (a) Arithmetic mean profile and spatial cross section of Conservative Temperature Θ. (b) Geometric mean profile and spatial cross section of stratification N^2. For the mean profiles, alternating colored background shading indicates the approximate depth ranges of the hydrographic layers defined in the text (PW, WH, and AW are labeled). For the spatial sections, the horizontal axis is broken and consecutively labeled 1–4 at the waypoints marked in Fig. 1, indicating where the glider changed direction. The white-outlined rectangle in (a) indicates the mesoscale eddy discussed in the text.

throughout this study, as appropriate. Confidence intervals for the computed mean and median values are reported in this paper as [–, –], representing lower and upper bounds based on the 95% confidence interval from bootstrap resampling in the case of arithmetic mean and median values, and the standard error in the mean derived from the geometric standard deviation in the case of geometric mean values.

3. Hydrography

In Fig. 2, we present the fields of Conservative Temperature Θ and squared buoyancy frequency $N^2 = -(g/\rho_\theta)\partial\rho_\theta/\partial z$. Here g is the gravitational acceleration and ρ_θ is the potential density referenced to the sea surface, derived from the CTD measurements and smoothed by a 15-s running mean filter when used in the calculation of N^2. For each field, a mean vertical profile and a spatial cross section are shown. The horizontal coordinate in the cross sections is the glider's geographic along-track distance coordinate s measured along the two-dimensional track shown in Fig. 1b. To guide the eye, each cross section is broken into multiple panels at waypoints where the glider changed its direction of travel.

We observe five distinct hydrographic layers, similar to those used to describe layering in the Canada Basin (e.g., Carmack et al. 1989). From shallowest to deepest, these are a warm surface mixed layer (SML), a strongly stratified near-surface cold halocline (CH), a cold Pacific Water (PW) layer, an intermediate warm halocline (WH) where temperature increases with depth, and a warm Atlantic Water (AW) layer. We define the boundaries of the layers using their local Conservative Temperature and Absolute Salinity S_A structure using criteria similar to those described in Jones (2001), Jackson et al. (2010), and Timmermans et al. (2014); the boundaries and hydrographic characteristics of the layers we observe are summarized in

TABLE 1. Properties of the hydrographic layers. Layers are defined by their Conservative Temperature Θ and Absolute Salinity S_A. The ranges given for depth, Conservative Temperature Θ, potential density anomaly σ_0, and stratification N^2 are for the central 90% of the data. The layer labels are SML: surface mixed layer; CH: cold halocline; PW: Pacific Water layer; WH: warm halocline; AW: Atlantic Water layer.

Layer	S_A (g kg^{-1})	Depth (m)	Θ (°C)	σ_0 (kg m^{-3})	N^2 (10^{-4} s^{-2})
SML	<28.3	0–14	From 5.9 to 7.3	21.2–22.1	—
CH	28.3–32.0	12–47	From −1.2 to 6.6	22.3–25.8	0.81–49.9
PW	32.0–33.2	47–122	From −1.4 to −0.6	25.9–27.1	0.41–2.45
WH	33.2–34.8	126–275	From −1.36 to 0.07	27.3–29.1	0.18–1.46
AW	>34.8	267——	From 0.15 to 0.36	29.1–29.8	0.03–0.31

Brought to you by HELMHOLTZ-ZENTRUM HEREON | Unauthenticated | Downloaded 04/22/21 12:14 PM UTC

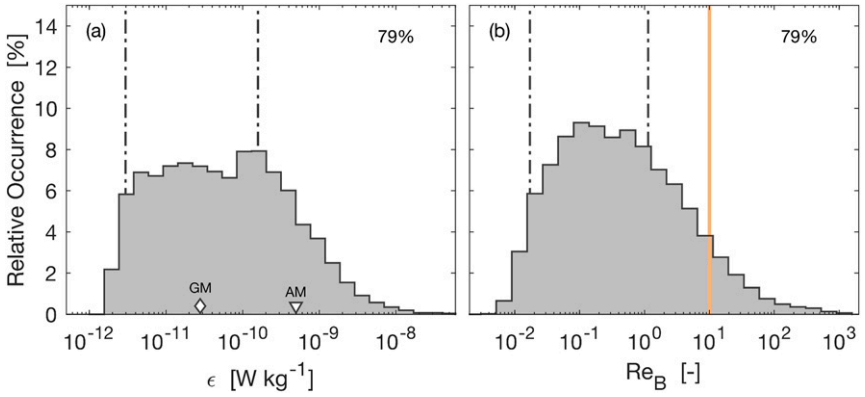

FIG. 3. Histograms of (a) the turbulent dissipation rate ε and (b) the buoyancy Reynolds number Re_B. For each, the number in the top right indicates the percentage of data that fall within the axis limits; the remaining data are below the detection limit and are not displayed. The interquartile range for each set, including below-detection-limit data, is the span between the two dash–dotted vertical lines. For ε, the geometric and arithmetic mean values are also indicated (GM and AM, respectively). For Re_B, the approximate critical value $\mathrm{Re}_B^* = 10$ is indicated by the yellow vertical line.

Table 1. The layering can be seen most easily in the Conservative Temperature profile (Fig. 2a).

Three points about the hydrography stand out as noteworthy for the purposes of this study. First, the amount of heat sequestered below the warm halocline in the warm AW layer is substantial: in the central gulf, where the water depth is ~425 m and the AW layer is $\Delta z \approx 160$ m thick and has a mean Conservative Temperature $\overline{\Theta}_{\mathrm{AW}} = 0.30°\mathrm{C}$, the sequestered heat E is approximately

$$E = \rho_0 c_p (\overline{\Theta}_{\mathrm{AW}} - \Theta_0)\Delta z \approx 2 \times 10^8 \ \mathrm{J\ m^{-2}}, \qquad (2)$$

relative to the melting Conservative Temperature of ice, $\Theta_0 = 0°\mathrm{C}$. Here the constants ρ_0 and c_p are characteristic values of the density and specific heat capacity of seawater, respectively, taken to be $\rho_0 = 1025\ \mathrm{kg\,m^{-3}}$ and $c_p = 3850\ \mathrm{J\,kg^{-1}\,°C^{-1}}$. If mixed or advected to the surface, this heat could melt $Z^* = 0.66$ m of sea ice, where $Z^* = E/(\rho_i L_o)$; $\rho_i = 910\ \mathrm{kg\,m^{-3}}$ is the density of sea ice (Timco and Frederking 1996) and $L_o = 3.3 \times 10^5\ \mathrm{J\,kg^{-1}}$ is the latent heat of melting sea ice (Ono 1967). This amount of sea ice loss would be a significant fraction of the Amundsen Gulf's mobile winter ice pack, which is typically 0.6–1.9 m thick in late spring (Peterson et al. 2008).

Second, the stratification is strong everywhere in the subsurface relative to that in lower-latitude oceans. Typical values for N^2 in the North Atlantic and North Pacific pycnoclines are $O(10^{-6})\ \mathrm{s^{-2}}$ (Emery et al. 1984). This benchmark is comparable to the smallest N^2 values we observe in the AW but is nearly two orders of magnitude smaller than N^2 in the PW layer and is three orders of magnitude smaller than N^2 in the CH. Numerous previous studies in the Beaufort Sea (e.g., Guthrie et al. 2013; Lincoln et al. 2016; Chanona et al. 2018) have noted that stratification is a key controlling feature of the mixing characteristics in this region. We will build on these results in section 4 by combining our measurements of the turbulence and density fields to demonstrate that density stratification frequently inhibits turbulent mixing in our dataset.

While most of the subsurface appears to be generally uniform in the horizontal plane, we observe substantial horizontal mesoscale and smaller [$O(1)$ km] Conservative Temperature variability in the PW layer (Fig. 2a). Most distinctive is the presence of a mesoscale eddy between waypoints 2 and 3. This variability and its potential implications for the layer's heat budget are discussed further in section 5c.

4. Turbulence and mixing

a. Turbulent dissipation rates

As is typical for ocean turbulence observations (e.g., Gregg 1987; Lueck et al. 2002), we observe an ε distribution that spans many orders of magnitude. Further, the positive skew in the distribution (Fig. 3a) suggests a relatively small number of strongly turbulent events occurring in a less turbulent background flow field. We note that the tail on the left side of the distribution is artificially cut off by the estimated noise floor of our microstructure temperature measurements: values of ε below the detection limit (21% of the data; section 2b), representing turbulence too weak for us to observe, are set to zero for the calculation of arithmetic mean and median values, and are not depicted in Fig. 3a. Resolvable ε realizations vary over five orders of magnitude, from $O(10^{-12})$ to $O(10^{-8})$ W kg^{-1}. The interquartile range (IQR) of these estimates is $(3.0\text{–}160) \times 10^{-12}\ \mathrm{W\,kg^{-1}}$.

Consistent with previous studies in the region (e.g., Bourgault et al. 2011; Guthrie et al. 2013; Rippeth et al. 2015; Lincoln et al. 2016), we find that turbulence is typically very weak. The geometric mean dissipation rate, representing the central tendency of a lognormally distributed variable, is 2.8 [2.7,

Brought to you by HELMHOLTZ-ZENTRUM HEREON | Unauthenticated | Downloaded 04/22/21 12:14 PM UTC

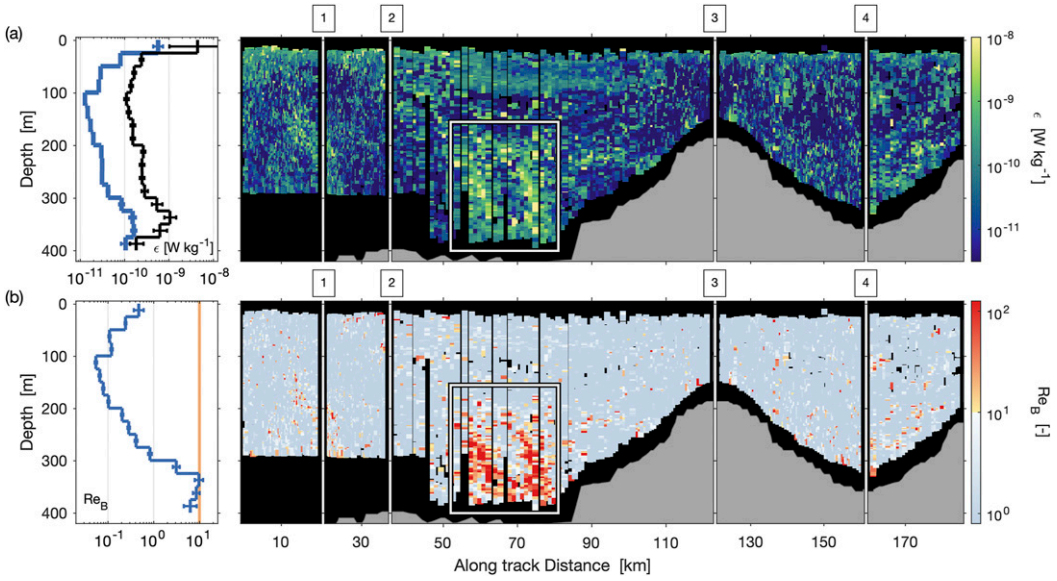

FIG. 4. Mean vertical profiles and horizontal cross sections of (a) ε and (b) Re_B. Waypoints are indicated as in Fig. 2. For each, the geometric mean profile is given in 25-m bins (blue), with error bars indicating the standard error in the mean using the geometric standard deviation; for ε, the arithmetic mean profile is also given (black), with error bars indicating the 95% confidence interval based on bootstrap resampling. As for all geometric mean values presented, below-detection limit values set to zero for all other calculations are set to the detection limit (2.0×10^{-12} W kg^{-1}) for the calculation of the geometric mean. In both cross sections, the white-outlined rectangle between waypoints 2 and 3 identifies the patch of enhanced turbulence discussed in the text. In the Re_B cross section, red pixels indicate where a turbulent diapycnal flux is expected and gray pixels indicate an expected absence of turbulent diapycnal mixing. The approximate critical value $\mathrm{Re}_B^* = 10$ is indicated in the Re_B mean profile by the vertical yellow line.

2.8] $\times$ 10^{-11} W kg^{-1}.[1] The median value is 2.3 [2.2, 2.4] $\times$ 10^{-11} W kg^{-1}. In 68% of these observations, ε is smaller than 1.0×10^{-10} W kg^{-1}, a common benchmark for "low turbulence" open ocean dissipation rates (Gregg 1999; Lueck et al. 2002). Only 0.4% of the distribution lies above 1×10^{-8} W kg^{-1}. However, the small number of large ε estimates do play an important role in setting the integrated dissipation rate over the period of observation: the arithmetic mean value of ε is 4.9 [4.0, 6.8] $\times$ 10^{-10} W kg^{-1}, more than an order of magnitude larger than the geometric mean and median values.

The variability of the ε field has a notable spatial structure that can be identified in the mean vertical profiles and horizontal cross section of the field (Fig. 4a). In the vertical, there is an ε minimum in the core of the cold PW layer at ~100-m depth: here ε is typically $O(10^{-11})$ W kg^{-1}. The geometric average dissipation rate near the sea surface and the seafloor indicates that ε is typically an order of magnitude larger in proximity to these boundaries. Consistent with the dataset as a whole, the arithmetic mean in each of these depth bins is an order of magnitude larger than the geometric mean (the arithmetic mean of ε is 4.4 [1.0, 20] $\times$ 10^{-9} W kg^{-1} at ~20-m depth, 1.1 [0.98, 1.2] $\times$ 10^{-10} W kg^{-1} at ~110-m depth, and 1.1 [0.79 1.4] $\times$ 10^{-9} W kg^{-1} at ~350-m depth). Larger uncertainty bounds in the mean of the near-surface bin reflects a stronger influence of high-end outliers of the distribution there. Laterally, the most obvious source of variability is a prominent near-bottom patch of elevated dissipation at the base of the continental slope, where ε can be as high as $O(10^{-8})$ W kg^{-1}. This turbulent patch is found between s = 52 and 81 km and is identified in Fig. 4a by a white-outlined rectangle.

Dissipation rates in the turbulent patch are anomalously high relative to the rest of the field but modify the statistics of the full dataset only marginally (Table 2). For example, the arithmetic mean of ε excluding estimates from within the patch is 4.4 [3.4, 6.3] $\times$ 10^{-10} W kg^{-1}, only 10% smaller than the estimate from the dataset as a whole. However, the arithmetic mean of data only from within the patch is 11 [9.7, 13] $\times$ 10^{-10} W kg^{-1}, an increase by a factor of 2.2 over the mean calculated from the full set of data. For a similar comparison of the geometric mean value, median value, and IQR see Table 2.

[1] Note that the geometric mean is defined only for nonzero values, so we set below-detection-limit values to the detection limit (2.0×10^{-12} W kg^{-1}) for geometric mean calculations throughout. We note that arithmetic mean and median values are not sensitive to the treatment of below-detection-limit estimates: these values are unchanged (to the number of significant figures reported) if these estimates are set to zero or the detection limit. In contrast, the geometric mean value can be sensitive to the treatment of below-detection-limit values: for example, the geometric mean value of ε for the full dataset reduces from 2.8 [2.7, 2.8] $\times$ 10^{-11} to 1.7 [1.6, 1.7] $\times$ 10^{-11} W kg^{-1} if these estimates are set to be the detection limit and an order of magnitude smaller than the detection limit value, respectively.

Brought to you by HELMHOLTZ-ZENTRUM HEREON | Unauthenticated | Downloaded 04/22/21 12:14 PM UTC

TABLE 2. Select statistics of ε and $|K_\rho|$ observed in all of the data, all data except that within the turbulent patch, and data only from within the turbulent patch. The turbulent patch is defined as the region inside the white-outlined rectangle in Figs. 4 and 7, between $s = 52$ and 81 km on the horizontal axis. Bracketed numbers indicate lower and upper bounds based on the 95% confidence interval from bootstrap resampling in the case of arithmetic mean and median values and the standard error in the mean from the geometric standard deviation in the case of geometric mean values.

	Arithmetic mean	Geometric mean	Median	IQR
		All data		
ε (10^{-11} W kg^{-1})	49 [40, 68]	2.8 [2.7, 2.8]	2.3 [2.2, 2.4]	0.30–16
$\lvert K_\rho\rvert$ (10^{-8} m^2 s^{-1})	450 [230, 1400]	0.87 [0.86, 0.89]	0.78 [0.76, 0.80]	0.25–1.6
		Excluding turbulent patch		
ε (10^{-11} W kg^{-1})	44 [34, 63]	2.4 [2.4, 2.5]	1.9 [1.8, 2.0]	0.30–13
$\lvert K_\rho\rvert$ (10^{-8} m^2 s^{-1})	100 [86, 140]	0.68 [0.67, 0.69]	0.70 [0.68, 0.72]	0.23–1.5
		Turbulent patch only		
ε (10^{-11} W kg^{-1})	110 [97, 130]	15 [14, 16]	18 [16, 21]	2.7–79
$\lvert K_\rho\rvert$ (10^{-8} m^2 s^{-1})	4600 [1800, 18 000]	17 [16, 19]	1.8 [1.8, 1.9]	1.1–810

Further information about the variability in the ε field is available from the glider's three repeat transects over the continental shelf slope. A comparison of the depth-averaged dissipation rate estimates along the three transects is shown in Fig. 5, for each of which ε is plotted as a function of distance from the glider's easternmost waypoint, geometrically averaged in 2.5-km bins. This bin-averaged dissipation rate remained of the same order of magnitude over the 7 days needed to complete the transects (note that the ε axis in Fig. 5 is linear, not logarithmic) and varied between (1–5) $\times$ 10^{-11} W kg^{-1}. From the first and last transects, it appears that ε is systematically larger in the central gulf than it is on the shelf slope, but the second transect does not exhibit this pattern; nonetheless, when all transects are averaged together (not shown), the pattern of enhanced ε in the central gulf relative to on the shelf slope remains. Note that the turbulent patch discussed previously and identified in Fig. 4 by the white-outlined rectangle is situated to the immediate left of the leftmost axis limit in Fig. 5.

A notable attribute of the ε transects in Fig. 5 is a number of localized peaks in the depth-averaged ε value that appear in all three occupations of the transect at approximately the same horizontal position. Examples are the local maxima at ~5–7-, ~18–19-, and ~23-km distance. Note that it is not possible to decouple time and space variability in measurements taken from a glider transect; here, we have treated the ε observations as a spatial series in order to highlight what appear to be geographic features, but we will discuss temporal variability and its implications in section 5a.

b. *The influence of stratification*

Combining observations of ε with those of N^2 and the kinematic viscosity ν, we construct estimates of the buoyancy Reynolds number, $\mathrm{Re}_B = \varepsilon/(\nu N^2)$, which quantifies the energetic capacity of the flow to develop vertical overturns that lead to diapycnal mixing (Figs. 3b and 4b). Note that in our computation of Re_B we bin N^2 similar to ε, described in section 2b, after applying a 15-s running mean smoothing. The Re_B parameter is a measure of the relative separation between the Ozmidov and Kolmogorov scales, that is, the length scale over which turbulence first becomes confined by stratification and the length scale over which turbulence becomes dissipated by viscosity, respectively. On length scales between these scales (the inertial subrange) we expect turbulent kinetic energy transfer to follow a scale-free cascade and be responsible for overturning density structure. A small Re_B value thus indicates that viscosity is acting to directly dissipate the turbulent motions responsible for overturning, whereas a large Re_B value indicates that the large overturning scales are undamped by viscous dissipation. Evidence from laboratory, numerical and field studies suggests that the Re_B parameter has a critical value near $\mathrm{Re}_B^* = 10$, below which vertical overturns and diapycnal turbulent mixing are unlikely (Stillinger et al. 1983; Shih et al. 2005; Ivey et al. 2008; Bouffard and Boegman 2013).

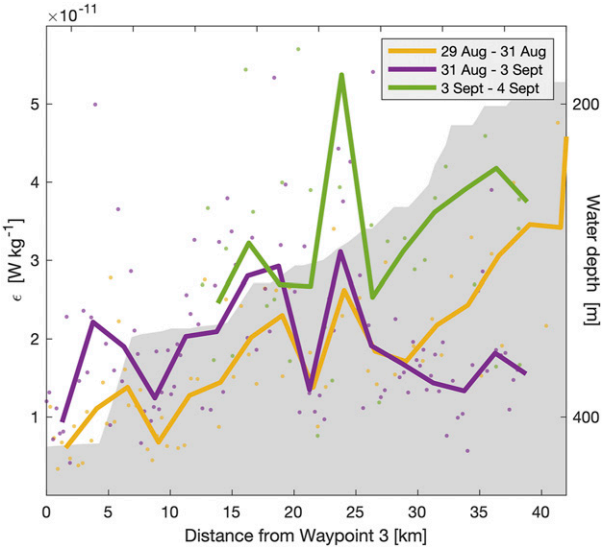

FIG. 5. The three repeat ε transects (left vertical axis) over the continental shelf slope. The horizontal axis is the distance from waypoint 3 shown in Fig. 1b. Thick lines are 2.5-km, geometric mean bin-averages of cast-averaged ε; colored markers in the background are the individual geometric mean cast averages. The bathymetry is shown with gray shading in the background (right vertical axis) for reference.

Brought to you by HELMHOLTZ-ZENTRUM HEREON | Unauthenticated | Downloaded 04/22/21 12:14 PM UTC

However, there is considerable debate as to whether an exact critical value exists, and on its possible dependence on parameters, with studies reporting a range of Re_B^* from as small as 0.1 up to 24 (Bouffard and Boegman 2013). In addition, our ability to accurately quantify ε at these small values of Re_B is questionable, especially due to the breakdown of the assumption of isotropic turbulence. Gargett et al. (1984) showed that the assumption of isotropic turbulence can break down at Re_B values as large as 200 and greater. We proceed to use low Re_B estimates with caution, keeping in mind their potential limitations.

We impose an $\mathrm{Re}_B^* = 10$ criterion to separate our data into two regimes, one in which turbulent diapycnal mixing is expected ($\mathrm{Re}_B \geq 10$), and one in which it is not ($\mathrm{Re}_B < 10$). Doing so, we find that turbulence in the flow is expected to be energetic enough to support enhanced turbulent diapycnal mixing for only 7% of our ε estimates; these are the estimates to the right of the yellow vertical line in Fig. 3b. Equivalently, we can say that we do not expect enhanced turbulent mixing in 93% of observations; in this large subset of the data we expect that the rates of molecular diffusion are relevant to the vertical fluxes of properties like temperature and salt. The Re_B distribution, therefore, suggests that stratification plays a dominant role in inhibiting turbulent mixing in the Amundsen Gulf at this time, suppressing the development of turbulence in the majority of our observations.

Further, it is apparent from the mean vertical profile and spatial cross section of the Re_B field (Fig. 4b) that where turbulent mixing is expected to occur is not homogeneously distributed in space. Rather, most of the turbulent mixing expected in our dataset occurs within 100 m of the seafloor in the isolated patch of enhanced ε that we observed at the edge of the shelf slope region (i.e., inside the white-outlined rectangles in Fig. 4). Only here is Re_B commonly of $O(10)$ or larger, with individual values occasionally reaching as large as $O(10^3)$. The white-outlined rectangle representing the region of enhanced ε in Fig. 4a encloses only 8% of ε estimates, but it encloses 41% of the occurrences where $\mathrm{Re}_B \geq 10$ and 64% of those where $\mathrm{Re}_B \geq 100$. Inside the rectangle, 37% of the ε estimates indicate that $\mathrm{Re}_B \geq 10$; in contrast, only 5% of the estimates indicate that $\mathrm{Re}_B \geq 10$ outside this region.

c. *Density diffusivity estimates*

In the 7% of observations where $\mathrm{Re}_B \geq 10$, we expect that turbulence drives a localized enhanced density flux. For these estimates, we calculate the rate of diapycnal density diffusion, K_ρ, using the canonical Osborn (1980) model for turbulent mixing:

$$K_\rho = \Gamma \frac{\varepsilon}{N^2}, \tag{3}$$

where Γ is a flux coefficient that we take to be 0.2 following Osborn's original (upper bound) estimate.

In the remaining 93% of observations, where $\mathrm{Re}_B < 10$ and a turbulent density flux is unlikely, temperature and salt are expected to diffuse by molecular diffusion. Assuming a linear approximation for the equation of state of seawater, the diffusivity of density in this case is given by

$$K_\rho = \frac{R_\rho \kappa_S^{\mathrm{mol}} - \kappa_T^{\mathrm{mol}}}{R_\rho - 1}, \tag{4}$$

where $\kappa_T^{\mathrm{mol}} = 1.4 \times 10^{-7}\ \mathrm{m^2\,s^{-1}}$ and $\kappa_S^{\mathrm{mol}} = 1.0 \times 10^{-9}\ \mathrm{m^2\,s^{-1}}$ are the molecular diffusion rates of temperature and salt in seawater. Defining the diffusivity ratio, $\tau = \kappa_S^{\mathrm{mol}}/\kappa_T^{\mathrm{mol}} = 1/140$, this expression can be written as

$$K_\rho = \frac{(R_\rho - \tau^{-1})}{R_\rho - 1} \kappa_S^{\mathrm{mol}}. \tag{5}$$

The quantity R_ρ is the gradient density ratio, defined as

$$R_\rho \equiv \frac{\beta(\partial S_A/\partial z)}{\alpha(\partial \Theta/\partial z)}, \tag{6}$$

where α and β are the coefficients for thermal expansion and haline contraction of seawater, respectively. Note that K_ρ here may be either positive or negative, depending on the sign and magnitude of R_ρ. Specifically, when $1 < R_\rho < \tau^{-1}$ (the case in 67% of our observations where $\mathrm{Re}_B < 10$), the density flux due to molecular diffusion of temperature and salt is downward, in the direction of increasing density. Note also that the water column becomes susceptible to double diffusion when R_ρ is low, a phenomenon that we have neglected here; we address the role of double diffusion in section 5b.

A histogram of the density diffusivity estimates, separated into upgradient and downgradient subsets, is given in Fig. 6a. The discontinuity between 8×10^{-8} and $3 \times 10^{-6}\,\mathrm{m^2\,s^{-1}}$ reflects the distinction between our estimates of K_ρ that assume turbulent mixing versus molecular diffusion, with all estimates to the right of the discontinuity computed using Eq. (3) and all estimates to the left of the discontinuity computed using Eq. (5). The discontinuity is an artifact of the Osborn model's inability to describe the transition between turbulent and nonturbulent density fluxes. Although alternative models that describe a smooth transition between the turbulent and molecular regimes have been proposed (e.g., Bouffard and Boegman 2013), the treatment of these transitional regime estimates do not have a significant impact on the characterization of the integrated diffusivity: arithmetic K_ρ averages are largely unaffected by variability (or inaccuracies) in the smaller orders of magnitude K_ρ estimates. To illustrate, we compare the arithmetic mean of all K_ρ estimates using the Osborn model [Eq. (3)] indiscriminately versus imposing the Re_B^* criterion to separate turbulent and nonturbulent mixing regimes: the arithmetic mean increases by a factor of only 1.1. For the same reason, negative K_ρ estimates are largely immaterial to the characterization of the arithmetic mean diffusivity: the negative K_ρ estimates are multiple orders of magnitude smaller than the few large (and positive) turbulent K_ρ estimates seen on the right-hand side of the K_ρ distribution that primarily set the arithmetic mean diffusion rate.

The arithmetic mean of all K_ρ estimates is 4.5 [2.3, 15] $\times 10^{-6}\,\mathrm{m^2\,s^{-1}}$, three orders of magnitude larger than the arithmetic mean of the molecular regime estimates (-3.8 [-3.9, -3.7] $\times 10^{-9}\,\mathrm{m^2\,s^{-1}}$). This implies that the upper 7% of K_ρ estimates

Brought to you by HELMHOLTZ-ZENTRUM HEREON | Unauthenticated | Downloaded 04/22/21 12:14 PM UTC

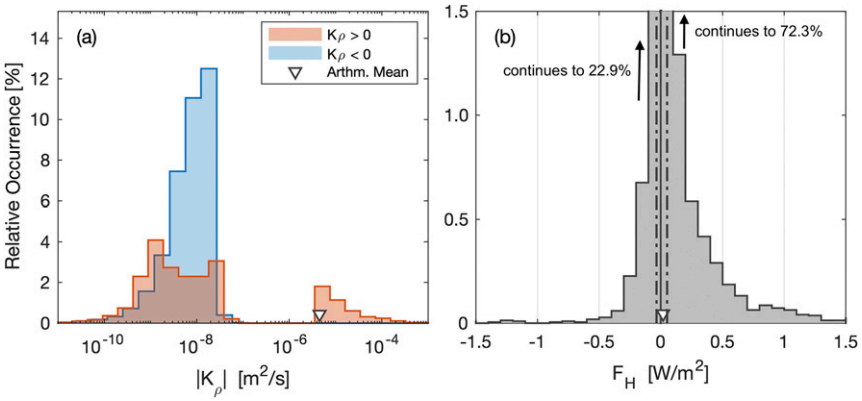

FIG. 6. Histogram of (a) the diapycnal mixing coefficient for density K_ρ for all nonzero measurements and (b) the vertical heat flux F_H for turbulent regime ($\mathrm{Re}_B \geq 10$) estimates only. Positive K_ρ indicates downgradient density diffusion; negative K_ρ indicates upgradient density diffusion. The arithmetic mean of all K_ρ estimates is indicated. For F_H, the dash–dotted lines indicate the 5th and 95th percentiles.

are responsible for drawing up the average mixing rate by a factor of approximately 2000 from that set by 93% of the observations in the molecular regime, a result that highlights the importance of the relatively small number of turbulent mixing events in setting the mean mixing rate. The arithmetic mean represents the 94th percentile of data: another indication of the disproportionate importance of the turbulent fluxes in setting the bulk transformation of buoyancy.

Like the dissipation rate, K_ρ shows systematic vertical structure (Fig. 7a; left panel): it is typically smallest at the depths of the cold PW layer around 100-m depth; it is typically one to three orders of magnitude larger near the surface and near the bottom. In these spatial views (Fig. 7a), K_ρ is computed locally as either a turbulent or molecular regime contribution as appropriate given the local Re_B value; the mean vertical profile averages the molecular and turbulent contributions accounting for their relative occurrence as a function of depth bin. The disproportionate contribution of a few, large turbulent mixing rate estimates is again apparent when comparing the geometric mean vertical profile of K_ρ to its arithmetic mean counterpart: the arithmetic mean profile is everywhere one to two orders of magnitude larger. In the upper 200 m of the water column, only 3% of the observations indicate a turbulent density flux. However, the arithmetic mean value of K_ρ is typically $O(10^{-7})$ $\mathrm{m^2\,s^{-1}}$, two orders of magnitude above the geometric mean value. Below 200-m depth, the arithmetic average of K_ρ increases steadily and reaches a maximum of $3.3 \times 10^{-5}\,\mathrm{m^2\,s^{-1}}$ between 335- and 360-m depth. This elevated mean K_ρ signal reflects the influence of the near-bottom turbulent patch at the edge of the shelf slope that is seen in the ε and Re_B sections (Fig. 4): this turbulent patch is the dominant feature in the K_ρ cross-sectional variability (Fig. 7a, right panel). Inside this patch, where 37% of the estimates indicate a turbulent mixing regime (section 4b), the arithmetic mean K_ρ value is 4.6 [1.8, 18] $\times$ $10^{-5}\,\mathrm{m^2\,s^{-1}}$; in comparison, outside the patch, where only 5% of mixing estimates are characterized as turbulent, the arithmetic mean value of K_ρ is 1.0 [0.86, 1.4] $\times$ $10^{-6}\,\mathrm{m^2\,s^{-1}}$. Further metrics comparing K_ρ inside and outside the patch are presented in Table 2.

d. *Vertical heat fluxes*

We use the temperature microstructure measurements to estimate the turbulent diffusivity of temperature K_T from the Osborn–Cox relation (Osborn and Cox 1972):

$$K_T = \kappa_T^{\mathrm{mol}} C, \tag{7}$$

where C is the Cox number, defined as

$$C \equiv \frac{\left\langle |\nabla \Theta'|^2 \right\rangle}{\left(\overline{\partial \Theta / \partial z}\right)^2} = \frac{3\left\langle (\partial \Theta'/\partial x)^2 \right\rangle}{\left(\overline{\partial \Theta / \partial z}\right)^2}, \tag{8}$$

which we calculate from a mean background vertical Conservative Temperature gradient, $\overline{\partial \Theta / \partial z}$, and the along-path microscale temperature gradient $\partial \Theta'/\partial x$. The second equality comes from the assumption of isotropic turbulence. Angle brackets indicate ensemble averaging over the same segments and subsegments used for the ε calculations (section 2b), whereas the overbar represents an arithmetic mean over a single ε segment. Note that the numerator of C represents the variance of turbulent thermal fluctuation gradients and can be evaluated in any direction (including the glider path direction, x) when isotropic turbulence is assumed. Further note that K_T and K_ρ are not generally equivalent in our observations because of the possibility of differential diffusion of temperature and salt, especially at low Re_B (e.g., Smyth et al. 2005).

The Osborn–Cox relation is based on an assumed balance between the turbulent production of thermal fluctuation variance and its dissipation through molecular diffusion. In regions of low Re_B, we do not expect significant turbulent production, and the balance assumed in the Osborn–Cox relation is unlikely to hold (e.g., Gregg 1975). Therefore, in estimating the temperature diffusivity, we apply the Osborn–Cox relation [Eq. (8)] only to those observations with $\mathrm{Re}_B \geq 10$. For all

Brought to you by HELMHOLTZ-ZENTRUM HEREON | Unauthenticated | Downloaded 04/22/21 12:14 PM UTC

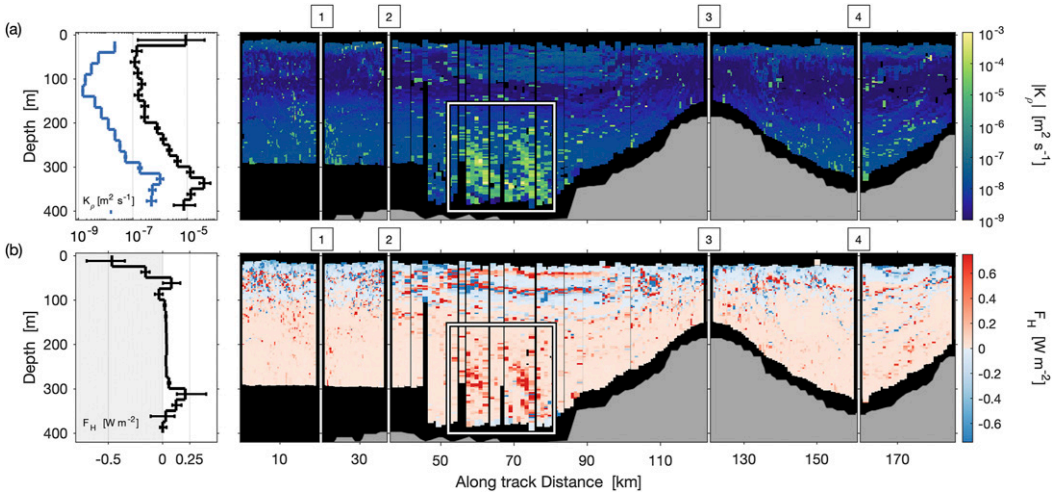

FIG. 7. Mean vertical profiles, in 25-m bins, and horizontal cross sections of (a) K_ρ and (b) F_H. For K_ρ, both geometric mean (blue) and arithmetic mean (black) profiles are shown; error bars indicate the standard error in the mean using the geometric standard deviation in the former and the 95% confidence interval based on bootstrap resampling in the latter. For F_H, the arithmetic mean profile is shown, with error bars indicating the 95% confidence interval based on bootstrap resampling. For the cross sections, the horizontal axis, waypoint markers, and white-outlined rectangle identifying the turbulent patch are as in Fig. 4.

remaining observations, we set the temperature diffusivity to the molecular value κ_T^{mol}. As only 7% of the measurements satisfy the $\text{Re}_B \geq 10$ condition for turbulent mixing (see section 4b), the majority of our heat flux estimates are considered to proceed at the molecular rate.

From estimates of temperature diffusivity, the vertical heat flux F_H is straightforward to obtain using

$$F_H = -\rho_0 c_p \kappa \frac{\overline{\partial \Theta}}{\partial z}. \tag{9}$$

Here the mixing rate κ is set to K_T where $\text{Re}_B \geq 10$ and to κ_T^{mol} elsewhere. The heat flux estimates we obtain are generally small (Fig. 6b): the IQR of $|F_H|$ is 0.003–0.01 W m^{-2}, and the absolute value of the flux, $|F_H|$, is less than 0.1 W m^{-2} in 95% of the observations. The arithmetic mean upward heat flux reaches as high as 0.18 [0.13, 0.26] W m^{-2} in the AW layer (Fig. 7b, left panel) because of the effects of the locally isolated turbulent patch (section 4a), which again is the dominant feature in the cross-section variability (Fig. 7b, right panel). However, even inside the patch, heat fluxes are modest: the arithmetic mean value of F_H here is 0.20 [0.16, 0.27] W m^{-2}, and F_H exceeds 1 W m^{-2} in only 3.5% of observations. The arithmetic mean heat flux through the warm halocline, separating the warm core of the AW and cold core of the PW, is an order of magnitude smaller. The magnitude of these mean heat flux values are low but comparable to previous observational estimates of $O(0.1)$ W m^{-2} in the central Canada Basin, where double diffusion often dominates the mixing (Padman and Dillon 1987; Timmermans et al. 2008a; Shibley et al. 2017), as well as to estimates of $O(0.1)$ to $O(1)$ W m^{-2} derived from observations on the Beaufort Sea shelf along the North American continent (Shaw et al. 2009; Chanona et al. 2018). Despite being comparable to previous estimates in the region, the magnitude of the mean heat flux observed in the turbulent patch is still two orders of magnitude smaller than the Arctic Ocean–wide mean rate of heat loss out of the AW of 6.7 W m^{-2} calculated by Turner (2010) based on a bulk estimate from the measurements of Aagaard and Greisman (1975). We note that the sources of this heat loss are still largely unaccounted for (Carmack et al. 2015).

5. Discussion: Mixing processes

a. Deep tidal mixing

In addition to geographic variability (section 4a), the deep ε field has a systematic temporal signal. This is seen in the power density spectrum of the ε observations (Fig. 8a), constructed by neglecting spatial variability and treating the glider measurements as a simple time series. Here we analyze a time series, shown in Fig. 8b, constructed by geometrically depth-averaging all ε observations deeper than 100-m depth, interpolating to a 15-min grid, and filtering to remove temporal variability on scales smaller than 2 h. To construct the spectrum, we use Welch's method using 4-day segments of data, 50% overlapped and Hamming-windowed. The most notable feature in the ε power spectrum is a rounded peak at frequencies spanning 1.3–2.4 cpd, straddling both the M_2 tidal frequency, 1.93 cpd, and the local inertial frequency, $f = 1.90$ cpd. The spectral peak thus suggests that the dominant mode of temporal variability in ε is linked to the semidiurnal tide, inertial forcing, or some combination of both.

Because of the close proximity of the frequencies of semidiurnal tides and the frequency of inertial currents at these latitudes, distinguishing internal tidal waves from inertial waves in this region is difficult. A number of results, however, suggest that tides are the dominant process setting the deep

Brought to you by HELMHOLTZ-ZENTRUM HEREON | Unauthenticated | Downloaded 04/22/21 12:14 PM UTC

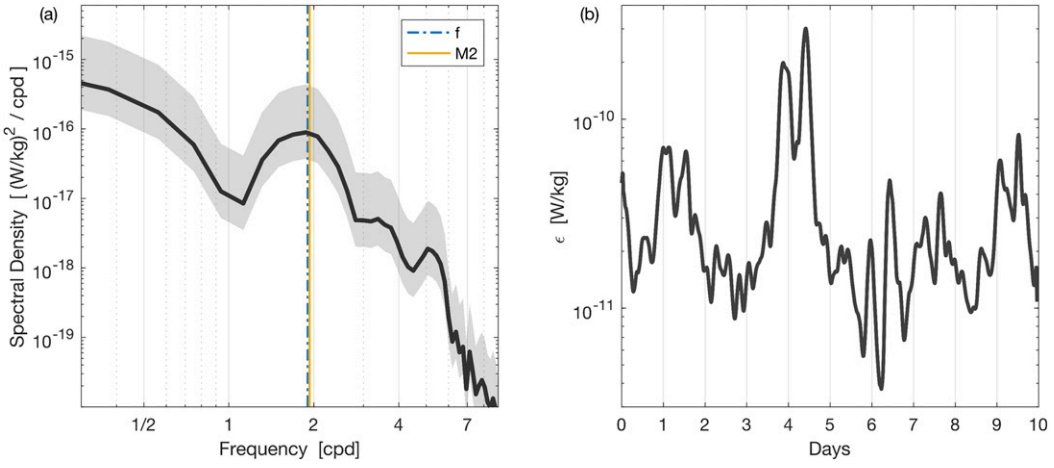

FIG. 8. (a) Power density spectrum of deep ε, constructed using Welch's method and 4-day segments of data. Gray shading indicates the 95% confidence interval. The M_2 tidal frequency and f are indicated by vertical lines. (b) The ε time series used to construct the power density spectrum. The series is made from the geometric cast averages of ε for all depths greater than 100 m and is interpolated to a 15-min grid. Variability on scales smaller than 2 h has been removed.

ε variability seen in Fig. 8. These include first the finding that no analogous peak in the ε power spectrum exists for observations shallower than 100-m depth (not shown); that is, the signal at the inertial and M_2 frequencies is only prevalent in the deeper measurements. It seems unlikely that the forcing of this deep signal originates at the surface (cf. Lincoln et al. 2016). Second, acoustic Doppler current profiler (ADCP) measurements from a nearby mooring (ArcticNet 2018 mooring CA08; Fig. 1b) show a slow and steady modulation of the barotropic (here depth-averaged between 10- and 170-m depth) velocity amplitude (Fig. 9a), suggesting that local current variability is predominantly tidal and not wind driven. Third, rotary spectra of the depth-averaged current velocities decomposed into tidal and nontidal components using tidal harmonic analysis (Pawlowicz et al. 2002) indicate that energy in both the clockwise and counterclockwise components centered at the f and M_2 frequencies is dominated by the energy in the tidal signal (Fig. 9b). Our analysis of the spatial distribution of turbulent dissipation (Fig. 5) further suggests a link between enhanced turbulence and topographic features, and thus a credible role of tidal modulation. Last, the directionality of both the deep tidal flow and the low-frequency residual current suggest that local tidally driven mixing is plausibly an important process at this site. Decomposing the deep currents into high-frequency and residual flows using a scale separation of 1.3 cpd, we find that the high-frequency flow (dominated by the tides, and accounting for 23% of the total variance) is predominantly aligned with the major axis of the Amundsen Gulf, as is the low-frequency residual flow that exceeds the tidal flow in magnitude (Fig. 9c). This setup is significant, because it implies that our study site is downstream of a region of complex topography offshore of the southern tip of Banks Island (Fig. 1a) roughly 2 times per day (i.e., the semidiurnal M_2 frequency).

Further support for the interpretation that ε is tidally modulated comes from the results of past studies in the region. We expect semidiurnal currents in the region to be strongly influenced by the locally generated baroclinic tide (Kulikov et al. 2010); the shelf slope north of nearby Cape Bathurst has previously been identified as a likely region of strong internal tide generation (Kulikov et al. 2004). A detailed analysis of tidal currents in the region by Kulikov et al. (2004) concluded that over 70% of the total energy of semidirunal currents was associated with baroclinic coherent tidal currents, as compared with only ~7% in association with inertial components. Furthermore, although the latitude of our study is southward of the critical latitude for the M_2 tide, it has been suggested that an M_2 internal tide generated in this region becomes resonantly trapped between the continent and the critical latitude (Kulikov et al. 2004, 2010). Ultimately, internal tides in this region are expected to dissipate near their generation site (Morozov and Pisarev 2002; Kulikov et al. 2004, 2010). We further note that observations linking tides and topography to mixing have been recently reported for the broader Arctic Ocean (Rippeth et al. 2015, 2017).

b. *Double diffusion*

Even when the mechanical energy inputs to mixing do not support enhanced turbulent mixing of buoyancy (section 4b), double diffusion can act to produce turbulent transports of temperature and salt (Radko 2013). The susceptibility of a water column to the diffusive regime of double diffusion can be characterized by the gradient density ratio R_ρ that is defined in section 4c. Empirically, diffusive convection in the Arctic Ocean is most commonly observed when $1 < R_\rho < 7$; it is also sometimes seen when $7 < R_\rho < 10$, but it is not typically observed when $R_\rho > 10$ (Shibley et al. 2017). In the central Canada Basin's warm halocline, R_ρ is typically 6.3 ± 1.4, and coherent double diffusive staircases are observed over horizontal scales exceeding 1000 km (Timmermans et al. 2008a; Shibley et al. 2017).

Brought to you by HELMHOLTZ-ZENTRUM HEREON | Unauthenticated | Downloaded 04/22/21 12:14 PM UTC

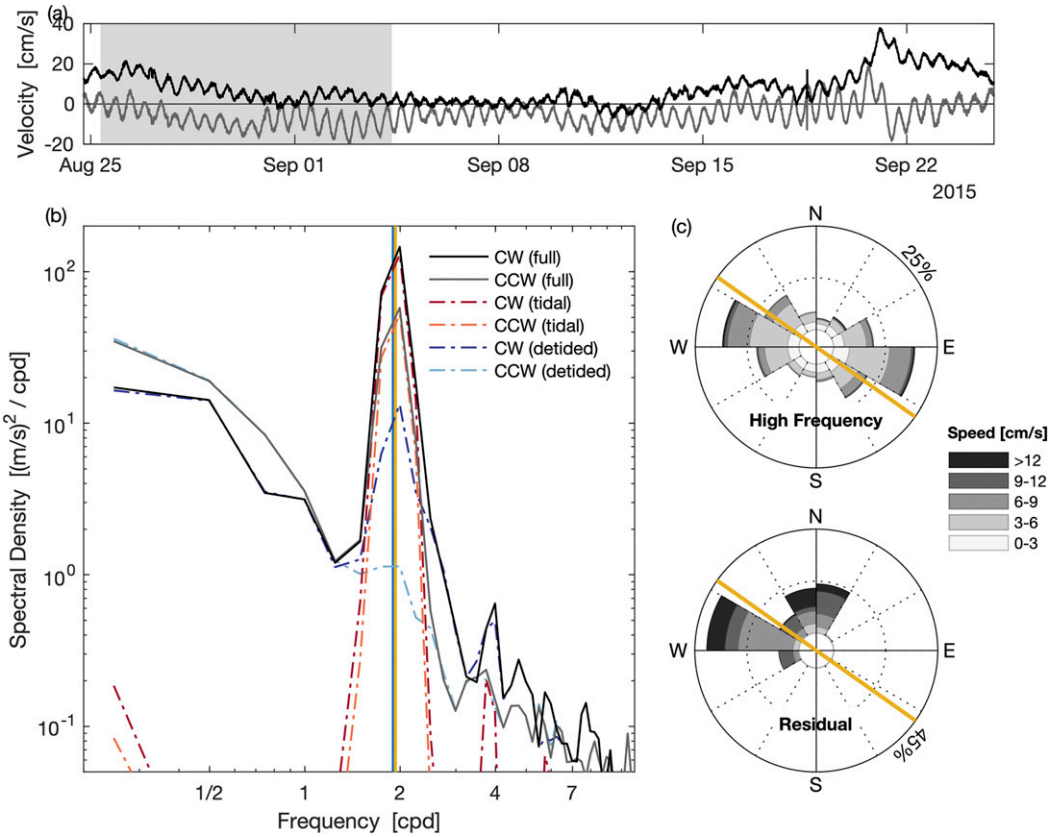

FIG. 9. (a) Depth-averaged current velocity components U (gray) and V (black) measured by ArcticNet mooring CA08 between 10- and 170-m depths. The light-gray shading indicates the period of the glider deployment. (b) Rotary spectra of the U and V records, as well as their decomposition into tidal and nontidal components, as indicated in the legend. The M_2 tidal frequency and f are indicated as in Fig. 8. (c) Polar histograms with current speeds of the U and V records, decomposed into high-frequency and residual components. High frequencies are defined as those greater than 1.3 cpd and are dominated by the M_2 tide. The approximate orientation of Amundsen Gulf's major axis, azimuth 305°, is indicated in each histogram by the yellow line. The percentage on each histogram's perimeter is the tick label for the radial axis (relative occurrence).

We calculate R_ρ from our measurements using background gradients filtered to exclude vertical scales smaller than 5 m (Fig. 10). We find that $1 < R_\rho < 10$ in 21% of observations; 19% are in the range 7–10, and 2% are in the range 1–7. Instances in which $1 < R_\rho < 10$ are almost exclusively in a band near the top of the Atlantic Water layer: in the potential density anomaly band $\sigma_0 = 28.5$–$29.5\ \mathrm{kg\,m^{-3}}$, corresponding approximately to the depth range ~200–335 m, 70% of R_ρ observations are in the range 1–10. There is also a notable number of small R_ρ values in the eddy, where 16% of R_ρ observations are in the range 1–10.

Despite conditions near the top of the AW layer that suggest that the density structure there could be favorable to double diffusion, we do not observe pervasive double diffusive staircases like those observed in the central Canada Basin's thermocline, although we do see sporadically dispersed individual temperature steps that are likely related to double diffusive processes. It appears, therefore, that double diffusion does not play a substantial role in the broader vertical transport of heat or density out of the thermocline in this region. This finding is potentially surprising at first because it is often thought that the absence of a double diffusive staircase implies energetic turbulent mixing (e.g., Guthrie et al. 2017; Shibley and Timmermans 2019), and the turbulent mixing estimates from our dataset are typically weak.

The absence of staircases could be due to a number of reasons. For example, more intense mixing upstream or earlier in time could plausibly explain staircase absence, especially given the region of complex topography upstream of the survey site and the variability of the low-frequency flow recorded by the CA08 mooring. It is also plausible that R_ρ is generally too large to lead to double-diffusive staircases, even in such a low-mixing environment. This situation is well documented in a number of deep lakes, where levels of $R_\rho \gtrsim 6$ are often found sufficient to prevent the formation of a well-defined staircase structure even in the complete absence of turbulent mixing (Wüest et al. 2012). Observations of staircases in the central Canada Basin thermocline (e.g., Padman and Dillon 1987; Timmermans et al. 2008a) are generally found at lower values of R_ρ than observed here.

Brought to you by HELMHOLTZ-ZENTRUM HEREON | Unauthenticated | Downloaded 04/22/21 12:14 PM UTC

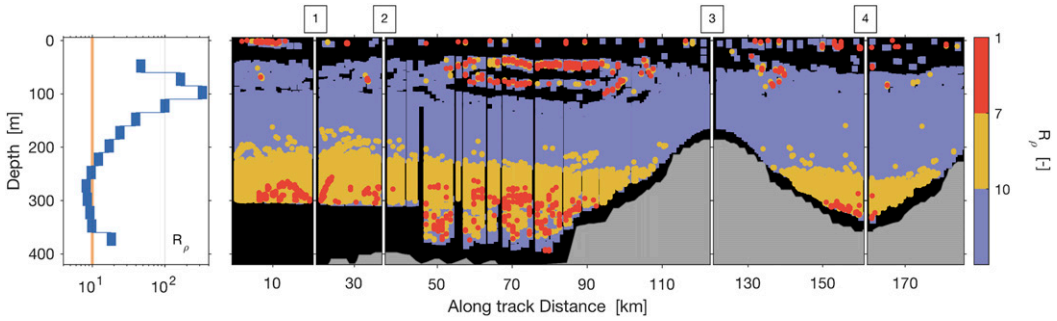

FIG. 10. Geometric mean vertical profile and horizontal cross section of the density ratio R_ρ. In the cross section, data are discretized into three regimes: susceptible to double diffusion (red: $R_\rho \leq 7$), marginally susceptible (yellow: $7 < R_\rho \leq 10$), and not susceptible (purple: $R_\rho > 10$). The value $R_\rho = 10$ is shown in the mean profile by the yellow vertical line.

c. *Pacific water mesoscale and smaller features*

One of the most striking features in our observations is the large variability in the temperature structure of the Pacific Water layer, visible in an enlarged view of the Conservative Temperature cross section (Fig. 11a). The most obvious feature here is the anticyclonic warm-core mesoscale eddy between along-track distances of $s = 53$ km and $s = 100$ km and depths of 40 and 110 m. The eddy has an approximate height of 70 m and an approximate diameter of 38 km; the latter dimension was estimated using the glider flight model of Merckelbach et al. (2019) to estimate the distance the glider traveled through water, and by assuming that the glider intersected the eddy's central core (see the appendix for details). With a maximum Conservative Temperature of −0.1°C observed at ~50-m depth, the eddy is about 1.3°C warmer than the ambient water at its core. It appears to have at least one outer tendril, transected by the glider twice at $s = 104$ km and $s = 139$ km along-track distance.

The origin of the eddy is unknown, but its large Conservative Temperature anomaly and Absolute Salinity range of 32–33 g kg^{-1} (Fig. 11b, right panel) suggest that it is composed of summer Bering Seawater (sBSW) that has been modified on the Chukchi shelf (Timmermans et al. 2014). Although the pathways of Chukchi shelf waters into the Beaufort Sea are highly variable, sBSW can form a component of the eastward shelfbreak jet (von Appen and Pickart 2012). These authors note that it is unlikely for sBSW to enter the Canadian Arctic Archipelago as a well-defined jet; rather it is expected that sBSW will enter in the form of mesoscale eddies derived from the jet through baroclinic and barotropic instabilities, consistent with what we observe. This life history suggests that the eddy may have originated from as far as along the shelf-break north of Alaska. Other known locations of mesoscale eddy formation in the Pacific Water layer include Cape Bathurst (Williams and Carmack 2008; Sévigny et al. 2015) and Mackenzie Canyon (Williams et al. 2006).

Irrespective of its possible origin, the eddy represents a significant amount of heat for the Amundsen Gulf. Assuming that the eddy is symmetric about a central axis, we estimate its total heat content to be 180 PJ (1 PJ = 10^{15} J) relative to the ambient water, taken to be $\Theta = -1.37$°C (see the appendix for details). When spread over the approximate area of Amundsen Gulf (taken as 400 km × 150 km), the heat from this eddy alone would be capable of producing a 1.0-cm depth of ice melt (see section 3), corresponding to 0.5%–1.7% of the late spring sea ice pack (Peterson et al. 2008). However, our observations suggest that turbulence in the Pacific Water layer is extremely weak and is generally insufficient to effect the upward turbulent transport of this heat to the sea ice cover above (section 4d). The absence of turbulence at these depths is reasonably expected to lead to the long-lived persistence of temperature anomalies in the PW layer such as the mesoscale eddy observed here.

Equally striking as the eddy is the presence of substantial temperature variability on horizontal scales of $O(1)$ km seen throughout the PW layer. This variability can be seen in Fig. 11a as a series of blotches superimposed on the ambient PW outside of the influence of the eddy. Temperature–salinity characteristics of these smaller-scale structures (Fig. 11b, middle panel) appear to be sufficiently dissimilar from those of the eddy that we suggest that they are distinct features, rather than tendrils of the eddy. It is unclear how these smaller structures were created. However, in light of recent results by Sévigny et al. (2015), who linked horizontal temperature structure above 100-m depth in Amundsen Gulf to submesoscale frontal formation and isopycnal outcropping at Cape Bathurst, it is possible that we are observing remnant features of nearby submesoscale dynamics.

6. Conclusions

Using a unique, near-continuous, 11-day glider-based sampling of turbulence and hydrography in Amundsen Gulf, a detailed quantification of turbulence and mixing led us to the following conclusions.

1) Consistent with previous studies in the region, we find that turbulence is typically very weak. In our dataset, the turbulent kinetic energy dissipation rate, ε, has a geometric mean value of 2.8×10^{-11} W kg^{-1} and is less than 1×10^{-10} W kg^{-1} in 68% of observations.

Brought to you by HELMHOLTZ-ZENTRUM HEREON | Unauthenticated | Downloaded 04/22/21 12:14 PM UTC

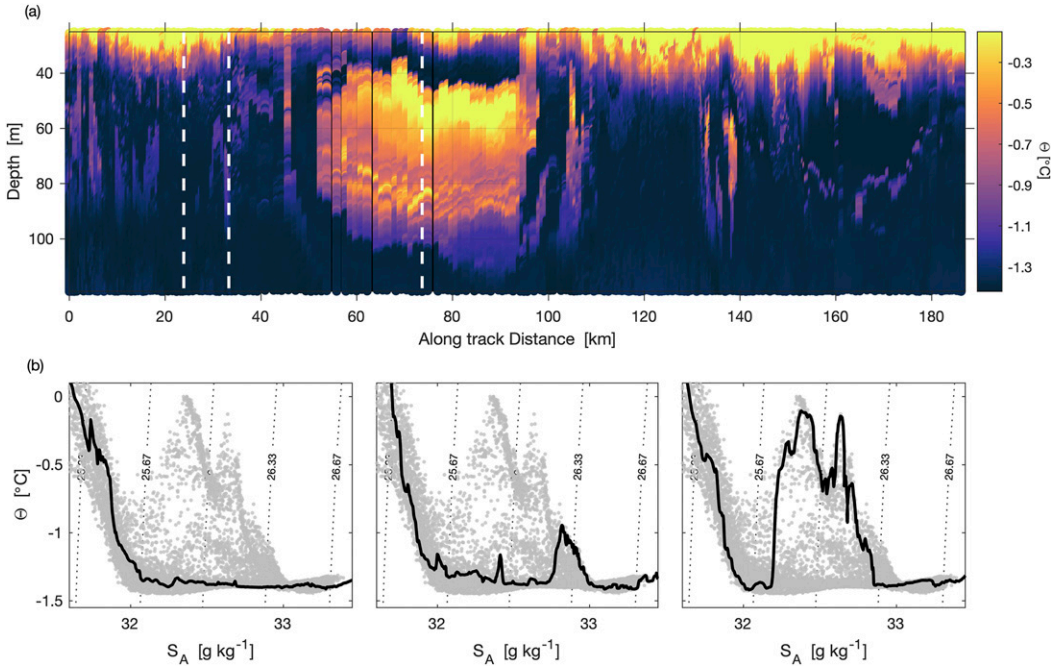

FIG. 11. (a) An enlarged view of the spatial cross section of Θ showing the cold halocline and Pacific Water layers, highlighting the eddy as well as smaller, $O(1)$ km, temperature anomalies. The vertical dashed white lines correspond, from left to right, to the three Θ–S_A lines shown in the three diagrams in (b). (b) The Θ–S_A diagrams for the three vertical profiles indicated (a). Gray dots are all of the data shown in (a). Dotted lines are potential density anomaly contours.

2) Further, we find that weak turbulence and strong stratification combine to predominantly inhibit turbulent diapycnal mixing of buoyancy in the region. The presence of turbulence strong enough to drive vertical overturns and an enhanced buoyancy flux above that expected from molecular diffusion, defined by the criteria $\mathrm{Re}_B \geq 10$, is found in only 7% of observations.
3) Despite typically weak turbulent levels, our dataset also shows that ε is highly variable, despite the limited time and space spanned by our measurements. Variability in ε in our observations spans five orders of magnitude.
4) An important implication of this variability is that a small number of strongly turbulent mixing events are disproportionately important in determining net buoyancy fluxes. These rare energetic turbulent events are responsible for enhancing the arithmetic mean diffusivity of density by three orders of magnitude above molecular levels.

The tightly resolved measurements of turbulence and hydrography also provided insight into the relevance of various possible turbulence-forcing mechanisms. We conclude the following.

1) Turbulent dissipation below the Pacific Water layer is modulated in time at the semidiurnal frequency and shows structure fixed in space across repeat transects over the continental shelf slope, suggesting that the deep turbulent field is tidally forced. Regional bathymetry and currents support the plausibility of this mechanism.
2) Despite weak turbulence levels and a density structure that is potentially favorable to double diffusion at the top of the Atlantic Water layer, we do not observe well-formed double diffusive structures. Thus, double diffusion does not appear to play a substantial role in the vertical transport of heat in this region at this time. However, the magnitude of the turbulent heat fluxes we estimate are comparable to those in the Canada Basin diffusive staircases, of order 0.1 $\mathrm{W\,m^{-2}}$.
3) Significant heat is present in the Pacific Water layer in the form of a mesoscale eddy and smaller scale structures; however, turbulent levels appear to be insufficient to cause a significant turbulent transport of this stored heat to shallower depths.

Given that the dominant forcing mechanism of deep turbulent mixing in the gulf has been proposed to occur through tide–topography interaction, it is relevant to pose the question of how representative our characterization of turbulence and mixing is for broader space and time scales than those spanned by our observations. The spatial variability of turbulence evident in our observations points to a possibly greater role played by regions of complex topography in setting the net mixing rate in the region, raising the question of whether broader scale measurements are needed to achieve a spatial sampling that leads to representative mixing statistics. Although the glider sampling provides improved statistics of the intermittent turbulent field, we also expect significant variability over longer time scales due to changes in wind and tidal forcing, residual current strength, ice conditions, and stratification, all of which have been shown to modulate internal wave energy and turbulence in the broader region (e.g., Dosser et al. 2014; Chanona et al. 2018; Cole et al. 2018). Low turbulence levels that these observations document

Brought to you by HELMHOLTZ-ZENTRUM HEREON | Unauthenticated | Downloaded 04/22/21 12:14 PM UTC

are consistent with finescale estimates of diffusivity in the Beaufort Sea in spring and summer over multiple years reported by Guthrie et al. (2013), but appear up to two orders of magnitude weaker than those measured in the gulf in early winter (Bourgault et al. 2011), the prime season for ventilating the mixed layer.

The role of turbulent mixing and its space–time variability in setting the vertical nitrate flux is important for Arctic Ocean primary production (e.g., Bourgault et al. 2011; Tremblay et al. 2015; Randelhoff and Guthrie 2016) and is thus particularly important to understand in the habitat of the Cape Bathurst Polynya (Stirling 1980, 1997) given the low turbulent mixing rates characterizing this region. Randelhoff and Guthrie (2016) report that regional differences in turbulent mixing and stratification lead to varying responses of primary production to climate change. We suggest that future glider-based sampling of turbulence in Amundsen Gulf and the Arctic Ocean more broadly has the potential to deliver a better understanding of time and space variability in mixing rates and its impacts, from which important insights with regard to the functioning of Arctic ecosystems in a changing climate may be gained.

Acknowledgments. The authors thank Lucas Merckelbach, Keith Lévesque, Dan Kelley, and the crew of the Canadian Coast Guard Ship *Amundsen*. They also thank Achim Randelhoff and two anonymous reviewers for critically reading the paper and making suggestions that led to significant improvements and clarifications. This work was supported by the National Science and Engineering Research Council of Canada (NSERC) through the Canadian Arctic GEOTRACES program—supported by the Climate Change and Atmospheric Research program (NSERC RGPCC 433848-12)—and the Discovery Grant Program (NSERC-2015-04866); the Helmholtz Foundation through the Polar Regions and Coasts in the Changing Earth System II program; the Alfred P. Sloan Foundation; the University of British Columbia; the Killam Doctoral Scholarships program; the Vanier Canada Graduate Scholarships program; the UBC Four Year Fellowship Program; the Northern Scientific Training Program; and the NSERC Michael W. Smith Foreign Study Supplement. Logistical support was provided by the Ocean Tracking Network (OTN); the Marine Environmental Observation, Prediction and Response (MEOPAR) Network; and the Amundsen Science Program, which are supported by the Canada Foundation for Innovation (CFI) and NSERC. Mooring data were collected on board the Canadian research icebreaker CCGS *Amundsen* for the Long-Term Ocean Observatory, a project of ArcticNet. MEOPAR and ArcticNet belong to the Networks of Centres of Excellence Program of the Government of Canada.

Data availability statement. ArcticNet data are publicly available on the Polar Data Catalogue. Replication data for this study are available online (https://doi.org/10.14288/1.0368671).

APPENDIX

Calculation of Eddy Geometry and Heat Content

Integration of the total heat content of the eddy required the following steps. First, it must be noted that the along-track distances quoted in the text, and denoted by s, are geographic distances relative to the fixed Earth frame. To estimate the diameter of the eddy, as well as a radial distance axis from the eddy center, the contribution of the water velocity acting to advect both the glider and the eddy over the fixed Earth coordinates must be accounted for. To do this, we have integrated the steady-state glider flight model of Merckelbach et al. (2019) in time, accounting for the heading of the glider, to produce a horizontal path of the glider through the eddy based on the glider's speed through the water. We next project this path onto a straight-line segment connecting the first and last positions at the eddy edges. We form a radial coordinate r by taking the central position of this line segment as the origin (allowing for negative r). Then, following similar studies (e.g., Armi et al. 1988; Fine et al. 2018), we assume that the eddy is axisymmetric and that the glider transected its center. This allows the heat content to be calculated through

$$\text{heat content} = \rho c_p \pi \int_{-R}^{R} |r| \int_{Z_{\text{eddy}}} [\Theta(r,z) - \Theta_{\text{ref}}]\, dz\, dr, \quad \text{(A1)}$$

where we allow the radial coordinate to range from $-R$ to R, with R being the eddy radius. This accounts for the fact that two halves of the eddy have been measured. Each half is revolved π radians in the axisymmetric assumption. The quantity Z_{eddy} represents the eddy height and is a function of r; Θ_{ref} is a reference temperature representing the temperature of the ambient water outside the eddy. We chose this to be −1.37°C. All values of $\Theta - \Theta_{\text{ref}} < 0$ are excluded from the integration, because this is considered to be ambient water. This calculation leads to an estimate of the eddy diameter of 38 km (as compared with a 48-km geographic along-track distance) and an estimate of the eddy heat content of 180 PJ, as stated in the main text.

REFERENCES

Aagaard, K., and P. Greisman, 1975: Towards new mass and heat budgets for the Arctic Ocean. *J. Geophys. Res.*, **80**, 3821–3827, https://doi.org/10.1029/JC080i027p03821.

ArcticNet, 2018: Amundsen Science Mooring Data Collection. Long-Term Ocean Observatory (LTOO) oceanographic mooring data collected in the Canadian Arctic Beaufort Sea. Accessed 28 August 2018, www.polardata.ca.

Armi, L., D. Hebert, N. Oakey, J. Price, P. L. Richardson, T. Rossby, and B. Ruddick, 1988: The history and decay of a Mediterranean salt lens. *Nature*, **333**, 649–651, https://doi.org/10.1038/333649a0.

Arrigo, K. R., and G. L. van Dijken, 2004: Annual cycles of sea ice and phytoplankton in Cape Bathurst polynya, southeastern Beaufort Sea, Canadian Arctic. *Geophys. Res. Lett.*, **31**, L08304, https://doi.org/10.1029/2003GL018978.

Baker, M. A., and C. H. Gibson, 1987: Sampling turbulence in the stratified ocean: Statistical consequences of strong intermittency. *J. Phys. Oceanogr.*, **17**, 1817–1836, https://doi.org/10.1175/1520-0485(1987)017<1817:STITSO>2.0.CO;2.

Bouffard, D., and L. Boegman, 2013: A diapycnal diffusivity model for stratified environmental flows. *Dyn. Atmos. Oceans*, **61-62**, 14–34, https://doi.org/10.1016/j.dynatmoce.2013.02.002.

Bourgault, D., C. Hamel, F. Cyr, J. É. Tremblay, P. S. Galbraith, D. Dumont, and Y. Gratton, 2011: Turbulent nitrate fluxes in

Brought to you by HELMHOLTZ-ZENTRUM HEREON | Unauthenticated | Downloaded 04/22/21 12:14 PM UTC

the Amundsen Gulf during ice-covered conditions. *Geophys. Res. Lett.*, **38**, L15602, https://doi.org/10.1029/2011GL047936.

Carmack, E., and R. W. MacDonald, 2002: Oceanography of the Canadian shelf of the Beaufort Sea: A setting for marine life. *Arctic*, **55**, 29–45, https://doi.org/10.14430/arctic733.

——, ——, and J. E. Papadakis, 1989: Water mass structure and boundaries in the Mackenzie shelf estuary. *J. Geophys. Res.*, **94**, 18 043–18 055, https://doi.org/10.1029/JC094iC12p18043.

——, and Coauthors, 2015: Toward quantifying the increasing role of oceanic heat in sea ice loss in the new Arctic. *Bull. Amer. Meteor. Soc.*, **96**, 2079–2105, https://doi.org/10.1175/BAMS-D-13-00177.1.

Chanona, M., S. Waterman, and Y. Gratton, 2018: Variability of internal wave-driven mixing and stratification in Canadian Arctic shelf and shelf-slope waters. *J. Geophys. Res. Oceans*, **123**, 9178–9195, https://doi.org/10.1029/2018JC014342.

Cole, S. T., J. M. Toole, L. Rainville, and C. M. Lee, 2018: Internal waves in the Arctic: Influence of ice concentration, ice roughness, and surface layer stratification. *J. Geophys. Res. Oceans*, **123**, 5571–5586, https://doi.org/10.1029/2018JC014096.

Dickson, D. L., and H. G. Gilchrist, 2002: Status of marine birds of the southeastern Beaufort Sea. *Arctic*, **55**, 46–58, https://doi.org/10.14430/arctic734.

Dosser, H. V., L. Rainville, and J. M. Toole, 2014: Near-inertial internal wave field in the Canada Basin from ice-tethered profilers. *J. Phys. Oceanogr.*, **44**, 413–426, https://doi.org/10.1175/JPO-D-13-0117.1.

Emery, W. J., W. G. Lee, and L. Magaard, 1984: Geographic and seasonal distributions of Brunt–Väisälä frequency and Rossby radii in the North Pacific and North Atlantic. *J. Phys. Oceanogr.*, **14**, 294–317, https://doi.org/10.1175/1520-0485(1984)014<0294:GASDOB>2.0.CO;2.

Fer, I., A. K. Peterson, and J. E. Ullgren, 2014: Microstructure measurements from an underwater glider in the turbulent Faroe Bank Channel Overflow. *J. Atmos. Oceanic Technol.*, **31**, 1128–1150, https://doi.org/10.1175/JTECH-D-13-00221.1.

Fine, E. C., J. A. MacKinnon, M. H. Alford, and J. B. Mickett, 2018: Microstructure observations of turbulent heat fluxes in a warm-core Canada Basin eddy. *J. Phys. Oceanogr.*, **48**, 2397–2418, https://doi.org/10.1175/JPO-D-18-0028.1.

Gargett, A., T. Osborn, and P. Nasmyth, 1984: Local isotropy and the decay of turbulence in a stratified fluid. *J. Fluid Mech.*, **144**, 231–280, https://doi.org/10.1017/S0022112084001592.

Grebmeier, J. M., and Coauthors, 2006: A major ecosystem shift in the northern Bering Sea. *Science*, **311**, 1461–1464, https://doi.org/10.1126/science.1121365.

Gregg, M. C., 1975: Microstructure and intrusions in the California Current. *J. Phys. Oceanogr.*, **5**, 253–278, https://doi.org/10.1175/1520-0485(1975)005<0253:MAIITC>2.0.CO;2.

——, 1987: Diapycnal mixing in the thermocline: A review. *J. Geophys. Res.*, **92**, 5249–5286, https://doi.org/10.1029/JC092iC05p05249.

——, 1999: Uncertainties and limitations in measuring ε and χ_T. *J. Atmos. Oceanic Technol.*, **16**, 1483–1490, https://doi.org/10.1175/1520-0426(1999)016<1483:UALIMA>2.0.CO;2.

——, M. H. Alford, H. Kontoyiannis, V. Zervakis, and D. Winkel, 2012: Mixing over the steep side of the Cycladic Plateau in the Aegean Sea. *J. Mar. Syst.*, **89**, 30–47, https://doi.org/10.1016/j.jmarsys.2011.07.009.

Guthrie, J. D., J. H. Morison, and I. Fer, 2013: Revisiting internal waves and mixing in the Arctic Ocean. *J. Geophys. Res. Oceans*, **118**, 3966–3977, https://doi.org/10.1002/jgrc.20294.

——, I. Fer, and J. H. Morison, 2017: Thermohaline staircases in the Amundsen Basin: Possible disruption by shear and mixing. *J. Geophys. Res. Oceans*, **122**, 7767–7782, https://doi.org/10.1002/2017JC012993.

Harwood, L. A., and I. Stirling, 1992: Distribution of ringed seals in the southeastern Beaufort Sea during late summer. *Can. J. Zool.*, **70**, 891–900, https://doi.org/10.1139/z92-127.

Ivey, G. N., K. B. Winters, and J. R. Koseff, 2008: Density stratification, turbulence, but how much mixing? *Annu. Rev. Fluid Mech.*, **40**, 169–184, https://doi.org/10.1146/annurev.fluid.39.050905.110314.

Jackson, J. M., E. C. Carmack, F. A. McLaughlin, S. E. Allen, and R. G. Ingram, 2010: Identification, characterization, and change of the near-surface temperature maximum in the Canada Basin, 1993-2008. *J. Geophys. Res.*, **115**, C05021, https://doi.org/10.1029/2009JC005265.

Jakobsson, M., and Coauthors, 2012: The International Bathymetric Chart of the Arctic Ocean (IBCAO) Version 3.0. *Geophys. Res. Lett.*, **39**, L12609, https://doi.org/10.1029/2012GL052219.

Jones, E. P., 2001: Circulation in the Arctic Ocean. *Polar Res.*, **20**, 139–146, https://doi.org/10.1111/j.1751-8369.2001.tb00049.x.

Khon, V. C., I. I. Mokhov, M. Latif, V. A. Semenov, and W. Park, 2010: Perspectives of Northern Sea Route and Northwest Passage in the twenty-first century. *Climatic Change*, **100**, 757–768, https://doi.org/10.1007/s10584-009-9683-2.

Kirkwood, T. B. L., 1979: Geometric means and measures of dispersion. *Biometrics*, **35**, 908–909.

Kulikov, E. A., A. B. Rabinovich, and E. Carmack, 2004: Barotropic and baroclinic tidal currents on the Mackenzie shelf break in the southeastern Beaufort Sea. *J. Geophys. Res.*, **109**, C05020, https://doi.org/10.1029/2003JC001986.

——, ——, and ——, 2010: Variability of baroclinic tidal currents on the Mackenzie Shelf, the southeastern Beaufort Sea. *Cont. Shelf Res.*, **30**, 656–667, https://doi.org/10.1016/j.csr.2009.11.006.

Lincoln, B. J., T. P. Rippeth, Y.-D. Lenn, M.-L. Timmermans, W. J. Williams, and S. Bacon, 2016: Wind-driven mixing at intermediate depths in an ice-free Arctic Ocean. *Geophys. Res. Lett.*, **43**, 9749–9756, https://doi.org/10.1002/2016GL070454.

Lueck, R. G., F. Wolk, and H. Yamazaki, 2002: Oceanic velocity microstructure measurements in the 20th century. *J. Oceanogr.*, **58**, 153–174, https://doi.org/10.1023/A:1015837020019.

Merckelbach, L., A. Berger, G. Krahmann, M. Dengler, and J. R. Carpenter, 2019: A dynamic flight model for Slocum gliders and implications for turbulence microstructure measurements. *J. Atmos. Oceanic Technol.*, **36**, 281–296, https://doi.org/10.1175/JTECH-D-18-0168.1.

Morozov, E., and S. V. Pisarev, 2002: Internal tides at the Arctic latitudes (numerical experiments). *Oceanology*, **42**, 165–173.

Niemi, A., J. Johnson, A. Majewski, H. Melling, J. Reist, and W. Williams, 2012: State of the ocean report for the Beaufort Sea Large Ocean Management Area. Canadian Manuscript Rep. of Fisheries and Aquatic Sciences Rep. 2977, 60 pp.

Ono, N., 1967: Specific heat and heat of fusion of sea ice. *Phys. Snow Ice: Proc.*, **1**, 599–610.

Osborn, T. R., 1980: Estimates of the local rate of vertical diffusion from dissipation measurements. *J. Phys. Oceanogr.*, **10**, 83–89, https://doi.org/10.1175/1520-0485(1980)010<0083:EOTLRO>2.0.CO;2.

——, and C. S. Cox, 1972: Oceanic fine structure. *Geophys. Fluid Dyn.*, **3**, 321–345, https://doi.org/10.1080/03091927208236085.

Padman, L., and T. M. Dillon, 1987: Vertical heat fluxes through the Beaufort Sea thermohaline staircase. *J. Geophys. Res.*, **92**, 10 799–10 806, https://doi.org/10.1029/JC092iC10p10799.

Palmer, M. R., G. R. Stephenson, M. E. Inall, C. Balfour, A. Düsterhus, and J. A. M. Green, 2015: Turbulence and

Brought to you by HELMHOLTZ-ZENTRUM HEREON | Unauthenticated | Downloaded 04/22/21 12:14 PM UTC

mixing by internal waves in the Celtic Sea determined from ocean glider microstructure measurements. *J. Mar. Syst.*, **144**, 57–69, https://doi.org/10.1016/j.jmarsys.2014.11.005.

Pawlowicz, R., B. Beardsley, and S. Lentz, 2002: Classical tidal harmonic analysis including error estimates in MATLAB using T TIDE. *Comput. Geosci.*, **28**, 929–937, https://doi.org/10.1016/S0098-3004(02)00013-4.

Peterson, A. K., and I. Fer, 2014: Dissipation measurements using temperature microstructure from an underwater glider. *Methods Oceanogr.*, **10**, 44–69, https://doi.org/10.1016/j.mio.2014.05.002.

Peterson, I. K., S. J. Prinsenberg, and J. S. Holladay, 2008: Observations of sea ice thickness, surface roughness and ice motion in Amundsen Gulf. *J. Geophys. Res.*, **113**, C060164, https://doi.org/10.1029/2007JC004456.

Post, E., and Coauthors, 2009: Ecological dynamics across the Arctic associated with recent climate change. *Science*, **325**, 1355–1358, https://doi.org/10.1126/science.1173113.

Prowse, T. D., C. Furgal, R. Chouinard, H. Melling, D. Milburn, and S. L. Smith, 2009: Implications of climate change for economic development in northern Canada: Energy, resource, and transportation sectors. *Ambio*, **38**, 272–281, https://doi.org/10.1579/0044-7447-38.5.272.

Radko, T., 2013: *Double-Diffusive Convection*. Cambridge University Press, 342 pp.

Rainville, L., and P. Winsor, 2008: Mixing across the Arctic Ocean: Microstructure observations during the Beringia 2005 Expedition. *Geophys. Res. Lett.*, **35**, L08606, https://doi.org/10.1029/2008GL033532.

——, C. Lee, and R. Woodgate, 2011: Impact of wind-driven mixing in the Arctic Ocean. *Oceanography*, **24**, 136–145, https://doi.org/10.5670/oceanog.2011.65.

Randelhoff, A., and J. D. Guthrie, 2016: Regional patterns in current and future export production in the central Arctic Ocean quantified from nitrate fluxes. *Geophys. Res. Lett.*, **43**, 8600–8608, https://doi.org/10.1002/2016GL070252.

Rippeth, T. P., B. J. Lincoln, Y.-D. Lenn, J. A. M. Green, A. Sundfjord, and S. Bacon, 2015: Tide-mediated warming of Arctic halocline by Atlantic heat fluxes over rough topography. *Nat. Geosci.*, **8**, 191–194, https://doi.org/10.1038/ngeo2350.

——, V. Vlasenko, N. Stashchuk, B. D. Scannell, J. A. M. Green, B. J. Lincoln, and S. Bacon, 2017: Tidal conversion and mixing poleward of the critical latitude (an Arctic case study). *Geophys. Res. Lett.*, **44**, 12 349–12 357, https://doi.org/10.1002/2017GL075310.

Ruddick, B., A. Anis, and K. Thompson, 2000: Maximum likelihood spectral fitting: The Batchelor spectrum. *J. Atmos. Oceanic Technol.*, **17**, 1541–1555, https://doi.org/10.1175/1520-0426(2000)017<1541:MLSFTB>2.0.CO;2.

Scheifele, B., S. Waterman, L. Merckelbach, and J. R. Carpenter, 2018: Measuring the dissipation rate of turbulent kinetic energy in strongly stratified, low-energy environments: A case study from the Arctic Ocean. *J. Geophys. Res. Oceans*, **123**, 5459–5480, https://doi.org/10.1029/2017JC013731.

Schultze, L. K. P., L. M. Merckelbach, and J. R. Carpenter, 2017: Turbulence and mixing in a shallow shelf sea from underwater gliders. *J. Geophys. Res. Oceans*, **122**, 9092–9109, https://doi.org/10.1002/2017JC012872.

Sévigny, C., Y. Gratton, and P. S. Galbraith, 2015: Frontal structures associated with coastal upwelling and ice-edge subduction events in southern Beaufort Sea during the Canadian Arctic Shelf Exchange Study. *J. Geophys. Res. Oceans*, **120**, 2523–2539, https://doi.org/10.1002/2014JC010641.

Shaw, W. J., and T. P. Stanton, 2014: Vertical diffusivity of the Western Arctic Ocean halocline. *J. Geophys. Res. Oceans*, **119**, 5017–5038, https://doi.org/10.1002/2013JC009598.

——, ——, M. G. McPhee, J. H. Morison, and D. G. Martinson, 2009: Role of the upper ocean in the energy budget of Arctic sea ice during SHEBA. *J. Geophys. Res.*, **114**, C06012, https://doi.org/10.1029/2008JC004991.

Shibley, N. C., and M. L. Timmermans, 2019: The formation of double-diffusive layers in a weakly turbulent environment. *J. Geophys. Res. Oceans*, **124**, 1445–1458, https://doi.org/10.1029/2018JC014625.

——, ——, J. R. Carpenter, and J. M. Toole, 2017: Spatial variability of the Arctic Ocean's double-diffusive staircase. *J. Geophys. Res. Oceans*, **122**, 980–994, https://doi.org/10.1002/2016JC012419.

Shih, L. H., J. R. Koseff, G. N. Ivey, and J. H. Ferziger, 2005: Parameterization of turbulent fluxes and scales using homogeneous sheared stably stratified turbulence simulations. *J. Fluid Mech.*, **525**, 193–214, https://doi.org/10.1017/S0022112004002587.

Shroyer, E., 2012: Turbulent kinetic energy dissipation in Barrow Canyon. *J. Phys. Oceanogr.*, **42**, 1012–1021, https://doi.org/10.1175/JPO-D-11-0184.1.

Smyth, W., J. Nash, and J. Moum, 2005: Differential diffusion in breaking Kelvin-Helmholtz billows. *J. Phys. Oceanogr.*, **35**, 1004–1022, https://doi.org/10.1175/JPO2739.1.

Stillinger, D. C., K. N. Helland, and C. W. Van Atta, 1983: Experiments on the transition of homogeneous turbulence to internal waves in a stratified fluid. *J. Fluid Mech.*, **131**, 91–122, https://doi.org/10.1017/S0022112083001251.

Stirling, I., 1980: The biological importance of polynyas in the Canadian Arctic. *Arctic*, **33**, 303–315, https://doi.org/10.14430/arctic2563.

——, 1997: The importance of polynyas, ice edges, and leads to marine mammals and birds. *J. Mar. Syst.*, **10**, 9–21, https://doi.org/10.1016/S0924-7963(96)00054-1.

Timco, G., and R. Frederking, 1996: A review of sea ice density. *Cold Reg. Sci. Technol.*, **24** (1), 1–6, https://doi.org/10.1016/0165-232X(95)00007-X.

Timmermans, M.-L., J. Toole, R. Krishfield, and P. Winsor, 2008a: Ice-Tethered Profiler observations of the double-diffusive staircase in the Canada Basin thermocline. *J. Geophys. Res.*, **113**, C00A02, https://doi.org/10.1029/2008JC004829.

——, ——, A. Proshutinsky, R. Krishfield, and A. Plueddemann, 2008b: Eddies in the Canada Basin, Arctic Ocean, observed from ice-tethered profilers. *J. Phys. Oceanogr.*, **38**, 133–145, https://doi.org/10.1175/2007JPO3782.1.

——, and Coauthors, 2014: Mechanisms of Pacific summer water variability in the Arctic's central Canada Basin. *J. Geophys. Res. Oceans*, **119**, 7523–7548, https://doi.org/10.1002/2014JC010273.

Tremblay, J.-E., L. G. Anderson, P. Matrai, P. Coupel, S. Belanger, C. Michel, and M. Reigsta, 2015: Global and regional drivers of nutrient supply, primary production and CO_2 drawdown in the changing Arctic Ocean. *Prog. Oceanogr.*, **139**, 171–196, https://doi.org/10.1016/j.pocean.2015.08.009.

Turner, J. S., 2010: The melting of ice in the Arctic Ocean: The influence of double-diffusive transport of heat from below. *J. Phys. Oceanogr.*, **40**, 249–256, https://doi.org/10.1175/2009JPO4279.1.

von Appen, W.-J., and R. Pickart, 2012: Two configurations of the Western Arctic shelfbreak current in summer. *J. Phys. Oceanogr.*, **42**, 329–351, https://doi.org/10.1175/JPO-D-11-026.1.

Wassmann, P., 2011: Arctic marine ecosystems in an era of rapid climate change. *Prog. Oceanogr.*, **90**, 1–17, https://doi.org/10.1016/j.pocean.2011.02.002.

Brought to you by HELMHOLTZ-ZENTRUM HEREON | Unauthenticated | Downloaded 04/22/21 12:14 PM UTC

——, 2015: Overarching perspectives of contemporary and future ecosystems in the Arctic Ocean. *Prog. Oceanogr.*, **139**, 1–12, https://doi.org/10.1016/j.pocean.2015.08.004.

Williams, W. J., and E. Carmack, 2008: Combined effect of wind-forcing and isobath divergence on upwelling at Cape Bathurst, Beaufort Sea. *J. Mar. Res.*, **66**, 645–663, https://doi.org/10.1357/002224008787536808.

——, ——, K. Shimada, H. Melling, K. Aagaard, R. W. Macdonald, and R. G. Ingram, 2006: Joint effects of wind and ice motion in forcing upwelling in Mackenzie Trough, Beaufort Sea. *Cont. Shelf Res.*, **26**, 2352–2366, https://doi.org/10.1016/j.csr.2006.06.012.

Wüest, A., T. Sommer, M. Schmid, and J. R. Carpenter, 2012: Diffusive-type of double diffusion in lakes—A review. *Environmental Fluid Mechanics: Memorial Volume in Honour of Prof. Gerhard H. Jirka*, W. Rodi and M. Uhlmann, Eds., IAHR Monographs, CRC Press, 271–284, https://doi.org/10.1201/b12283.

Brought to you by HELMHOLTZ-ZENTRUM HEREON | Unauthenticated | Downloaded 04/22/21 12:14 PM UTC